UNIVERSITÀ DEGLI STUDI DI PADOVA

UNIVERSITA' DEGLI STUDI DI PADOVA

Dipartimento di Ingegneria Industriale DII

Corso di Laurea Magistrale in Ingegneria dell'Energia Elettrica

Simulation models and experimental verification of losses in induction motor drives

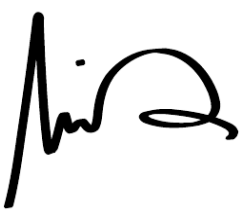

Relatore: Prof. Nicola Bianchi

Relatore: Prof. Fernando Briz del Blanco

Laureando: Tommaso Moretto (1156670)

Anno Accademico 2018/2019

Abstract

The objective of this thesis is to implement and test different tools that are able to predict induction machines' performances and compare the models prediction with the data measured experimentally.
Those models, or others versions refined in future research, could later be employed in the context of railway traction in order to compare the impact of different control and modulation strategies in the motor's performances.
We built a *finite element method* (FEM) model of an induction machine and compared its performance predictions with the ones of two others analytical models. This was carried out with sinusoidal and non-sinusoidal voltage excitation. For the tests with non-sinusoidal excitation were used low switching frequency waveforms, that are typically employed in the railway traction field.
Losses and torque estimations were compared in all these voltage scenarios.
A flux observer was implemented to post-process the FEM simulation data. Accurate prediction of torque harmonics via q axis current ones was carried out.
The FEM model was used to compare different alimentation conditions for the same mechanical operating point as well.
The modelled motor was mounted on a test bench and an experimental setup that allowed the measurements of electrical and mechanical (torque and angular speed) power was built.
Experimental tests only concerned the sinusoidal voltage excitation scenario.

Sommario

L'obbiettivo del presente lavoro consiste nell'implementazione e nella prova di diversi strumenti di predizione delle prestazioni di un motore asincrono, comparando poi i risultati forniti dalle simulazioni con i dati ricavati dalle misure sperimentali sulla macchina.
Questi modelli, o delle loro versioni affinate in un futuro lavoro di ricerca, trovano applicazione pratica nel contesto della trazione ferroviaria, dove sono impiegati per stimare l'impatto di diverse strategie di controllo e di modulazione sulle prestazioni del motore.
É stato costruito un modello agli elementi finiti (*finite element method*, FEM) di un motore ad induzione, le prestazioni(coppia, perdite nel rame e nel ferro) stimate da questo sono state comparate con quelle fornite da due diversi modelli analitici. Ció é stato eseguito impiegando tensioni di alimentazione sinusoidali e non sinusoidali. In questo secondo scenario sono state utilizzate forme d'onda, tipiche della trazione ferroviaria, caratterizzate dal ridotto valore della frequenza di commutazione impiegata dall'inverter per produrle.
É stato implementato un osservatore di flusso per eseguire un post-processing dei dati prodotti dalle simulazioni FEM. Si é dimostrata l'accuratezza nella predizione della armoniche di coppia tramite le armoniche di corrente di asse q.
Il modello agli elementi finiti é stato impiegato anche per comparare diverse condizioni di alimentazione per lo stesso punto di lavoro meccanico.
Il motore é stato montato in una bancata e si é realizzato un setup di misura che ha consentito l'acquisizione sperimentale dei valori di potenza elettrica e meccanica (coppia e velocità angolare).
I test sperimentali sono stati eseguiti impiegando solo alimentazione sinusoidale.

Contents

Listing of figures

Listing of tables

1

Introduction

Today's concerns about environment and the increasing energy demand despite the limited resources are constantly driving efficiency improvements in the electrical engineering field.
It's estimated that the 50% of the electrical energy produced worldwide is used by motors, mainly induction motors [1]. Research aiming at reducing the power losses in induction machines has been done for over 40 years [2].
The fact that those machines are employed in a wide range of different applications suggests that in specific ones there is room for efficiency improvement and even a little amelioration could lead to big global energy savings.

In the particular field of railway traction, where induction motors are extensively used, developing a cost-optimal traction system is a complex process in which exists the risk of sub-optimisation. Even in satisfying the simple requirement of a maximum running time between two stations with a certain train weight, various trade-offs must be taken care of. Among them we underline the "Inverter size vs Motor size".
It's possible to obtain the same torque speed characteristic of the drive using two different machine designs with different base speeds [3].
To some extent adapting a given motor to another $\frac{V}{f}$ characteristic is doable by means of a stator rewinding. In order to get a higher base speed the new winding requires less turns and a bigger cross section of the conductor.

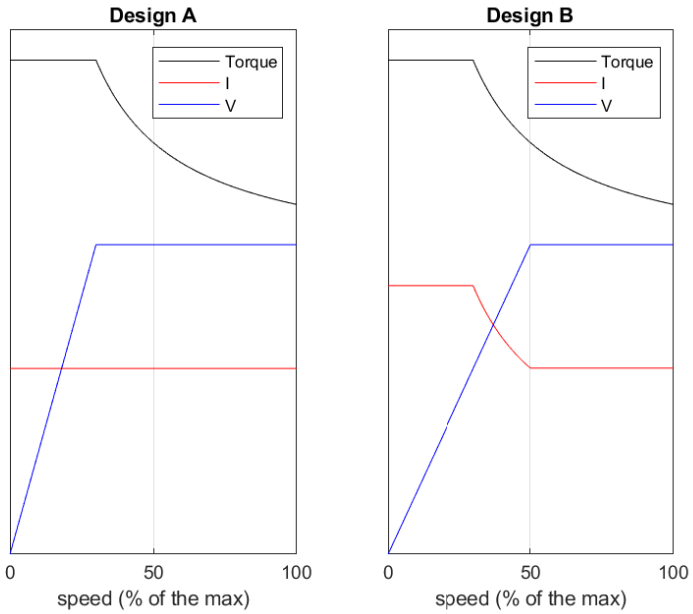

Figure 1.1: Design A (big motor, small inverter) and Design B (small motor, big inverter) characteristics comparison

A qualitative example of the two different designs, comparing torque, current and voltage versus speed characteristics is given in figure 1.1.

The design strategy aiming at enhancing the energy savings in railway traction focuses on increasing the machine's power density under the constraint of a fixed external diameter.
Operating possibilities for different rewinding configurations are detailed in the following section.
Increased power density in the motor can guarantee energy saving because of the higher regenerative brake power and the reduced powering running time that implies lower losses in the traction system [4].

Models describing the behaviour of induction machines are widely employed in industrial and academic fields.
They are fundamental for control and power electronics design as well as for overall losses minimization.
Generally, analytical models are the most suitable for flux observers and machine controllers in industrial applications, finite element modelling is useful to get more precise estimations of performance and compare different design choices.
Usually machines are designed for full load operation, and in this case the great majority of the losses are due to Joule effect, we will be referring to them as copper losses even though in the stud-

ied motor rotor Joule losses take place in aluminium bars. As the load decreases iron losses become gradually more relevant while copper ones decrease [5].
In order to estimate more precisely the performance of machines that operate frequently in low load condition accurate core losses modelling is crucial. This kind of operation interest machines used in railway traction, and to optimize its performance accurate core looses modelling is not to be neglected.

In this context the objective of this thesis is to implement and test tools that are able to predict induction machines' performances.
Those could find practical application in the railway traction field where being able to estimate losses precisely for specific load profiles would play a key role in optimizing control and modulation algorithms to enhance energy savings.
Induction motors used in railway traction are typically fed with voltages produced by inverters operating at low switching frequency, to give an idea of the voltage waveforms we can refer for example to low frequency *pulse width modulation* (PWM), six step or *selective harmonic elimination* (SHE) with a small number of switching angles per quarter period.
That being said, managing to predict performances with non sinusoidal voltage excitation is a major issue.

The models being studied here are not considering the thermal behaviour of the machine.
So the whole heat transfer process is not taken into account and temperature dependent parameters are considered as constants, computed at a specific temperature.

In this introduction, after having provided the overall context for this work, we proceed to describe the operation possibilities for induction machines with rewinded stator.

The following chapter describes the procedure adopted to build the *finite element method* (FEM) model of the machine. We mention the geometrical measurement process, describe the capabilities of the software employed and run some tests to compare performances. Different materials for lamination and rotor bars were investigated, as well as different values for the most difficult to measure geometrical quantities, took in the neighbourhood of the measured ones. The flux observer model implemented in the dynamic simulation software, employed for post-processing the FEM results, is presented as well. In the end it's outlined a procedure used to get a quick estimation of the real machine's parameters which are compared with the FEM extracted ones.

Chapter 3 hosts the comparison of performance prediction among analytical and FEM models,

referring to this last one as a benchmark. At first the two analytical models are described, then the parameters extraction procedure from the FEM model is outlined, lastly the performance predictions of the three models are compared in three different voltage waveform scenarios.

After a brief theoretical parentheses where the generation of torque harmonics due to current ones is outlined, chapter 4 goes on showing the comparison of torque waveform in time, and torque spectrum in the frequency domain, produced as an output by the FEM and the dynamic post-processing simulation. This is done for various voltage waveform scenarios. In the last section the accuracy of low frequency torque harmonics prediction using current ones is confirmed by operating a torque spectrum "cleaning" via q-axis current harmonics.

In the fifth chapter is carried out a comparison between different alimentation conditions that can cause the machine to work in the same mechanical operating point.
After describing the tuning procedure of the input data used to get the desired mechanical output, total losses and their four components are presented in graphs. This because losses will surely be one of the parameters playing a key role in the trade off for evaluating the optimum alimentation conditions.
Non-sinusoidal waveforms and different design configurations are not taken into account.

Chapter 6 deals with experimental tests. At first the test bench configuration, its mounting procedure and the measurement instrumentation employed are detailed.Later on we proceed to analyse torque spectra, computed starting from the output waveform of the torque sensor, relative to the operation of only the load motor, only the test one and both of them. We then proceed to describe the problem experienced with the drive that made impossible to work with the test motor as an actual motor and the load one regenerating. Finally are reported the performance measurements with the test motor generating at various rotor speeds (or, mutatis mutandis, slip values).

1.1 Operating Possibilities for "rewinded" machines

It is undoubtedly important to understand what possibilities rewinding the stator could offer.
We will consider two machines and analyse their steady state regions of operation.
The first one it's the original machine, no modification to its stator winding has been done. The second one is identical to the first, except for the stator winding. In the latter the stator was rewinded. The new winding presents half of the turns but double the cross section (or, in other words, diameter increased by a factor $\sqrt{2}$).
Doubling the cross section and reducing by half the length of the conductor implies that the two

stator windings present the same amount of copper. The differences between the original and the rewinded machine are summarized in table 1.1, different possibilities were analysed for the rewinded machine [10].

Machine configuration	1 (original)	2a (rewinded)	2b (rewinded)	2c (rewinded)
Conductor diameter	1	$\sqrt{2}$	$\sqrt{2}$	$\sqrt{2}$
Rated current (machine)	1	2	2	2
Rated voltage (machine)	1	0.5	1	1
Power rating (machine)	1	1	2	1
Machine size	1	1	1	< 1
DC link voltage	1	0.5	1	1
Rated current (inverter)	1	2	2	2
Power rating (inverter)	1	1	2	2

Table 1.1: Analysed design possibilities

In addition to what is listed in 1.1 is important to make other considerations. Subscript 1 will refer to the original machine, while 2 to the rewinded one.

- $Section_2 = \frac{1}{2} Section_1$
- $N_{turns,2} = \frac{1}{2} N_{turns,1}$
- $Length_2 = \frac{1}{2} Length_1$
- $R_2 = \frac{1}{4} R_1$
- $L_{S,2} = \frac{1}{4} L_{S,1}$
- $I_{N,2} = 2 I_{N,1}$, current density is the same

As a consequence of the considerations listed in the previous bullet list we can say that:

$\Rightarrow$ The two machines exhibits the same stator Joule losses in nominal operating conditions $P_{Cu,2} = P_{Cu,1}$ (even if the current doubles resistance is reduced to one fourth)

$\Rightarrow$ The second machine presents half of the stator flux linkage $\lambda_{S,2} = \frac{1}{2} \lambda_{S,1}$ (the inductance is reduced by four but the current doubles)

For the configuration 1 Torque reduction and flux weakening occur at the same speed, triggered by the voltage limit.

In the case $2a$ Voltage and current ratings of machine and inverter are changed according to the new stator winding configuration. Nominal current doubles and nominal voltage is reduced by half.
Such a machine could theoretically present the same output power of the original one. Torque and speed will be the same as in the first case. Voltage reduction is immediately justified by thinking about the parameters playing a role in the back electromotive force of a machine.
In nominal operating conditions only a small percentage of the voltage applied to the terminals of the motor drops in the stator resistance and leakage reactance. Since the Back-emf represents the great majority of the phase voltage of the motor, those voltage drops can be neglected in order to simplify qualitative analysis .
Since

$$\lambda_{S,2a} = \frac{1}{2}\lambda_{S,1}$$

$$\omega_{S,2a} = \omega_{S,1}$$

and

$$\left|\underline{\hat{V_{2a}}}\right| \approx BackEMF_{2a} = \omega_{e,2a} \cdot \left|\underline{\lambda_{S,2a}}\right|$$

$$\left|\underline{\hat{V_1}}\right| \approx BackEMF_1 = \omega_{e,1} \cdot \left|\underline{\lambda_{S,1}}\right|$$

it's immediately proven that

$$\left|\underline{\hat{V_{2a}}}\right| = \frac{1}{2}\left|\underline{\hat{V_1}}\right|$$

Case $2b$ is more a theoretical exercise useful for understanding rather than an actual viable configuration.
Here is assumed that the new winding can withstand the same voltage of the first one, while having half of the turns.
In this configuration the power rating could potentially double and the parameters defining power will vary in this way:

- Input power (Electrical), $P_{el,2b} = 2P_{el,1}$
  - $V_{2b} = V_1$
  - $I_{2b} = 2I_1$

- Output power (Mechanical), $P_{m,2b} = 2P_{m,1}$

- $T_{2b} = T_1$
- $\omega_{2b} = 2\omega_1$

In a similar way of what it has been shown before we can say that now, since

$$\lambda_{S,2b} = \frac{1}{2}\lambda_{S,1}$$

$$\omega_{S,2b} = 2\omega_{S,1}$$

we get

$$\left|\hat{\underline{V_{2b}}}\right| = \left|\hat{\underline{V_1}}\right|$$

This configuration is obviously not a viable one.

The greatest concern, from the electromagnetic point of view, will be core losses. In the case of sinusoidal excitation it's typical to express core loss density $\left[\frac{W}{m^3}\right]$ by means of the Steinmetz equation [11]:

$$P = k \cdot f^{\alpha} B^{\beta}$$

Where k is a material constant, f is the frequency and B is the peak value of the flux density. α and β are two parameters that depend on the material and are known to change significantly with frequency, flux density and waveforms.

Anyway for our goal here is enough to know that the exponent of frequency typically assumes values between 1 and 2.

On a qualitative level we can affirm that, even though the flux linkage is a half of the one of case 1, the flux density peak will be the same in every point of the machine.

In fact we are exciting the same magnetic circuit with the same ampere-turns, as we reduced by half the turns but doubled the current.

In order to operate the machine at $\omega_{S,2b} = 2\omega_{S,1}$ is necessary that the frequency doubles respect to case 1.

In this scenario doubling the frequency will cause the iron losses to grow more than the double, potentially quadratically. It's easy to imagine that the consequent temperature rise would be unacceptable.

Apart from this there would also be some issues from the mechanical point of view that would undermine the feasibility of this configuration.

Case $2c$ presents the same voltage and current ratings of $2b$ in this case the aim isn't to operate the machine at the double of the rated power. The desire is to take advantage of the control possibilities and efficiency improvements that the new configuration offers.
This could eventually lead to a redesign of the machine, a size reduction that translates in a power density increase.

2

Machine characterization

We now proceed describing how we built the FEM model of the machine. We will mention the geometrical measurement process, describe the capabilities of the software employed and run some tests to investigate the influence of materials and geometry on performance. Different materials for rotor bars were investigated, as well as different values for the most difficult to measure geometrical quantities.
The flux observer model implemented in the dynamic simulation software, employed for post-processing the FEM results, is presented as well.
Later on we outline a procedure used to get a quick estimation of the real machine's parameters which are compared with the FEM extracted ones.
In the end is described the stator rewinding process that was performed on two machines.

Table 2.1 reports the machine's nameplate data.

V	connection	Hz	rpm	kW	A	cos(ϕ)
230	D	50	1450	4.00	15.20	0.75
400	Y	50	1445	4.00	8.80	0.75
415	Y	50	1445	4.00	9	0.71

Table 2.1: Nameplate data

2.1 Geometry measurements for FEM modelling

A model of the original machine has been built in a FEM analysis software[1].
Since we didn't dispose of any data sheet regarding machine geometry nor materials, we took advantage of the rewinding process, that will be detailed later on this chapter, for measuring the stator slots geometry ad its internal diameter (see tab 2.2 and figures 2.1 and 2.2).
We owned three identical induction motors, so a rotor has been cut in order to measure properly the shape of the bars' cross section and the rotor lamination (figures 2.3 and 2.4).

All those measurements have been performed with a caliper, that guarantees a good accuracy for the biggest parts such as stack length, rotor diameter, shaft, etc.
Some others were difficult to perform and for them the accuracy is lower.
In this category fall the slot quantities in particular the slot openings of stator and rotor.
Another tricky thing is getting a precise estimation of the air gap.
This quantity is computed starting from the rotor and stator internal diameter $g = \frac{D_{s,int} - D_r}{2}$.
The internal diameter of the stator is not easily evaluated. To do so a micrometer was used, as is difficult to get a precise value of a diameter employing a caliper whose edges are straight surfaces.
After removing the rotor a flat surface was used to pose the micrometer and get a reasonably accurate measure of the diameter as shown in figure 2.2.

Stator slots	36
Rotor bars	26
Stack length	$159.55[mm]$
D yoke	$161.4[mm]$
D stator	$104.2[mm]$
D rotor	$103.4[mm]$
gap	$0.4[mm]$
D shaft	$35.35[mm]$
Ring length	$7.9[mm]$
Ring heigth	$19.65[mm]$

Table 2.2: Motor geometry

[1] The software employed for the FEM simulations is Ansys

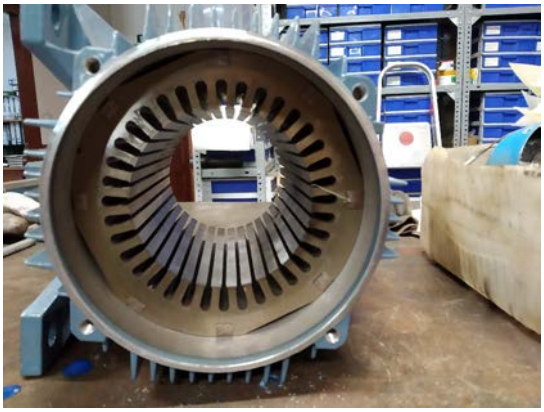

Figure 2.1: Stator without winding

Figure 2.2: Measuring of stator inner diameter

Figure 2.3: Half of the cut Rotor

Figure 2.4: Rotor lamination

2.2 FEM model

The model of the machine was built using the RMXprt tool.
This tool, starting from all the geomtrical, electrical and mechanical specification, is able to build a $2D$ model of the machine. The $2D$ modelization is chosen because of the smaller computational time required for the simulations compared to the $3D$ one. Anyways is important to underline that this model provide valid results as it takes into account the $Z - axis$ length of the machine and $3D$ effects like:

- End winding Leakage inductance (for the stator winding and for the rotor rings as well)
- End winding Resistance (for the stator winding and for the rotor rings as well)
- Rotor Bars Skewing

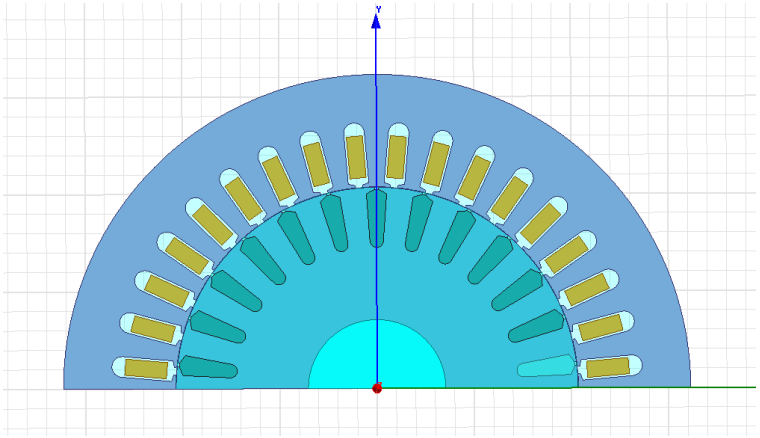

Figure 2.5: 2D FEM Model of half Induction motor

End winding Resistance and Leakage inductance are estimated analytically from machine Data (geometry and material characteristics).
The skewing model works by considering a certain number of "slices" of the actual machine, realizing a stepping skew. The results coming from each slice are combined to generate the solution.
As can be seen in figure 2.5 to slim the computational burden of the simulation, we took advantage of the symmetry of the problem and simulated only half of the machine.

Thanks to the rewinding operations it was possible to infer winding scheme and measure conductors diameter. This allowed to model the stator winding precisely.

From the cut end winding(figure 2.6) we inferred the scheme:

- Full pitch;
- 24 conductors per slot;
- 4 wires per conductor;
- Wire diameter ($0.65[mm]$).

To measure the true diameter of the conductor of a single wire, useful for modelling but also for rewinding the machine precisely, the insulation of a wire was removed by melting it with a flame and a micrometer was used(figure 2.7).

Figure 2.6: Head of the stator winding

Figure 2.7: Micrometer for measuring the conductor diameter

2.2.1 Materials influence

At this point it's worth to underline the difficulty of modelling the machine without knowing the materials characteristics.
Different lamination steels have an influence in the operating characteristics of the machine as well as rotor bars materials.

To get an idea of rotor bars material influence we compared the torque slip curves employing three different materials.
Simulations are run to compare aluminium, cast aluminium and cast aluminium with parameters computed at a temperature of $55°C$, this last one just to give an idea of the importance of the temperature dependent parameters.
The differences in the rotor resistance reflect in the Torque speed curve 2.8 and in the rated param-

eters data 2.3.
In this simulations the lamination material employed was M19 − 24G.

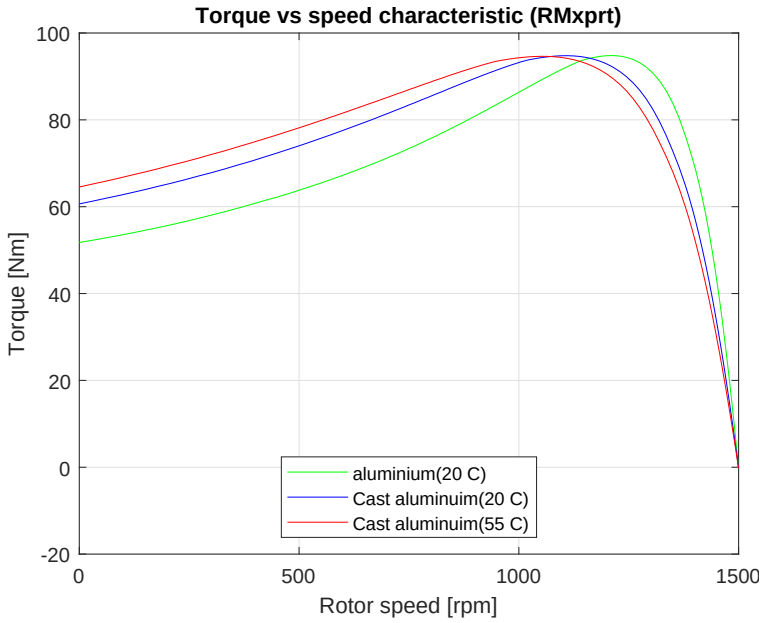

Figure 2.8: Torque slip curves comparison for different rotor bars materials

	Aluminium	Cast Aluminium(20[°C])
$\omega_r[rpm]$	1472	1462
$cos(\phi)$	0.62	0.62
$I_{stator}[A]$	10.8	10.8

Table 2.3: Rated load operation data (varying rotor bar material)

Not knowing precisely the material characteristics made us run some comparison tests among the materials available in the library of the software.
This means that for building the $2D$ FEM model were employed, for the lamination, M19 − 24G, and for the rotor bars Cast Aluminium($20°C$).
The chose of the lamination material was based on the close similarity of the *BH* characteristic to the ones commonly employed in the electrical machine design course [7].

2.2.2 Geometry parameters influence

As mentioned before measuring small quantities with the caliper implies an uncertainty on the measured value.

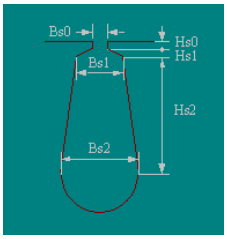

(a) Stator slot

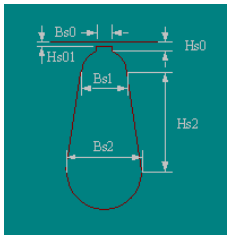

(b) Rotor slot

Figure 2.10: Slots geometric parameters

To analyse to which extent this can influence the behaviour of the simulated machine several simulations with different values of the geometrical parameters representing the stator and rotor slots were run.
Referring to picture 2.10, simulations were run multiplying for different scale factors (0.8, 0.9, 1, 1.1, 1.2) the parameters: $Bs0$, $Hs2$ and Tooth width for the stator slot, while for the rotor one: $Bs0$, $Hs2$, $Bs1$ and $Bs2$.
Tooth width parameter was multiplied for $\frac{1}{scalefactor}$, as the aim was to stretch, for scale factors > 1, and shrink, for scale factors < 1, the slot.

The following figures, 2.9 and 2.11, show the results of the simulations.

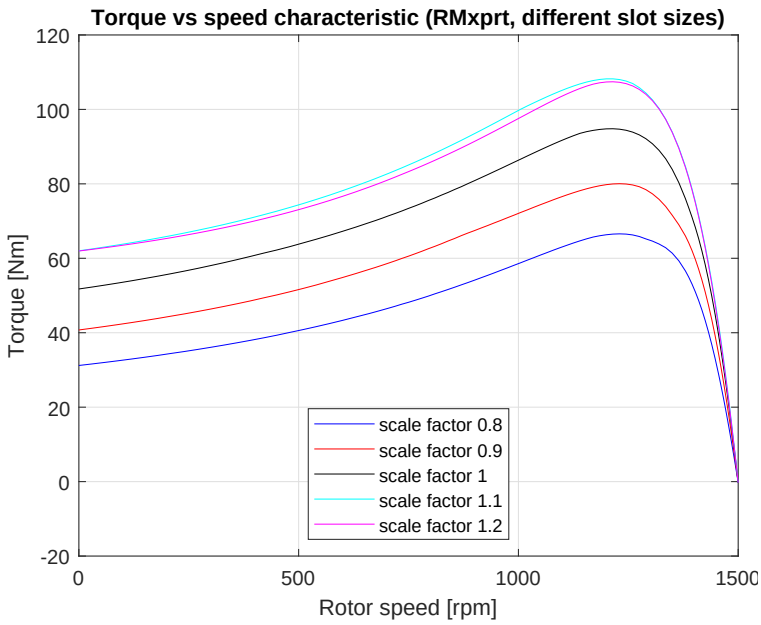

Figure 2.9: Torque vs speed curves comparison for different slots size

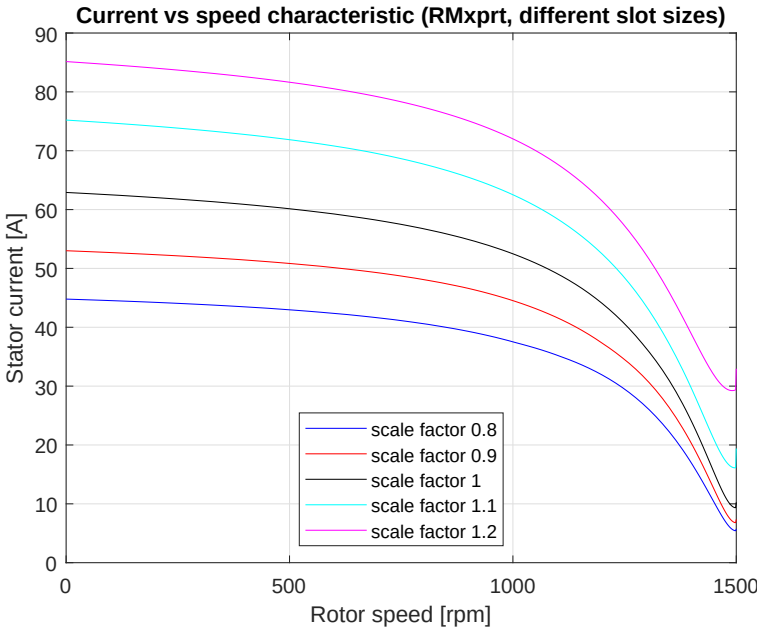

Figure 2.11: Current vs speed curves comparison for different slots size

2.3 Dynamic simulation model

A Dynamic simulation model[2] of the machine is used to validate the FEM analysis results. This model receives as input the voltage excitation waveform employed in the FEM and the consequent current to realize a post-processing validation.
It employs the Voltage Observer algorithm to estimate the rotor flux and the electromagnetic torque. The algorithm computes the stator flux by means of the equation 2.1, while the rotor flux spatial vector is reconstructed, in the stator reference frame, by the 2.2.

$$\boldsymbol{\lambda}_s^s = \int_{-\infty}^{t} (\boldsymbol{u}_s^s - R_s \boldsymbol{i}_s^s) dt \tag{2.1}$$

$$\boldsymbol{\lambda}_r^s = \frac{L_r}{L_M} \boldsymbol{\lambda}_s^s + \left(\frac{L_M^2 - L_s L_r}{L_M} \right) \boldsymbol{i}_s^s \tag{2.2}$$

Voltage observer is implemented in the stationary reference frame but to get the d and q axis currents the model presents a phase lock loop to estimate the rotor flux angle and allow the $\alpha\beta$ to dq transformation.
Electromagnetic torque is used as a check with the finite element method results since torque is an output of that simulation too.

[2] The software used for the dynamic simulations is Simulink

The block scheme in figure 2.12 underlines the input and output quantities of the model easening the understanding of how it works.
Red arrows indicates input quantities, while black ones are employed for outputs.

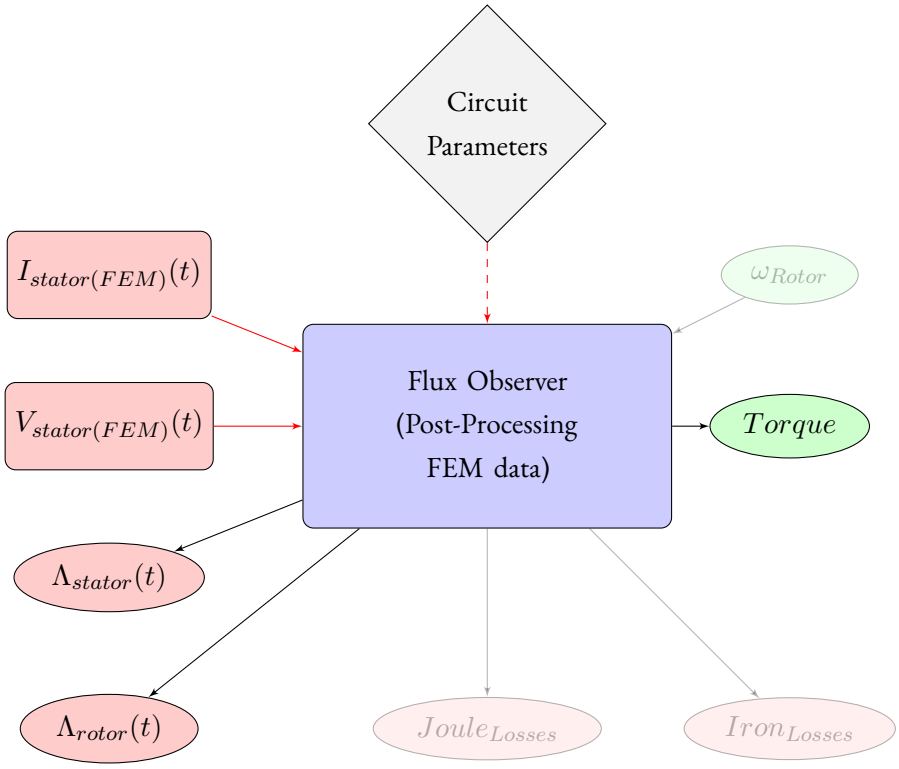

Figure 2.12: Flux Observer block diagram

2.4 Quick estimation of Motor Parameters

In order to get a rapid estimation of the induction motor parameters a "signal test" was performed. With the stator winding in star connection configuration, a step voltage was applied between a phase and the centre of the star of the winding.
The voltage step was produced by closing a switch placed in between a constant DC voltage source and a phase of the stator winding. Oscilloscope probes were used for measuring the voltage and the current in the winding.
In figure 2.13 is possible to see the oscilloscope acquisition relative to this test.

Data acquired from oscilloscope were imported in Matlab where with the help of the system identification toolbox it was possible to estimate the motor parameters.
This tool is able to identify a transfer function such that for a given input produces a given output,

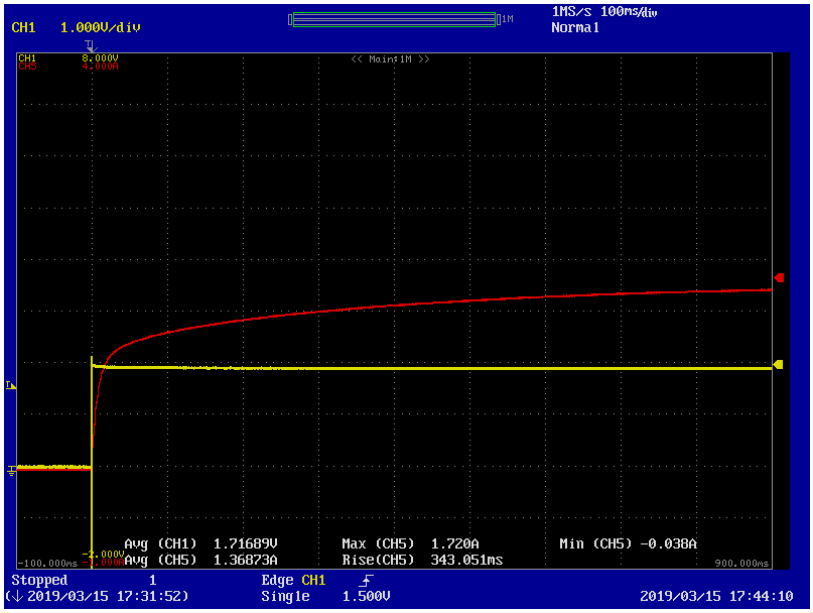

Figure 2.13: Step response of a Phase of the machine

feeding the voltage waveform as input and the current one as output the software identified a suiting transfer function.
Then it was supposed that, for the test we did, the circuit model in figure 2.14 was a suiting representation of system.

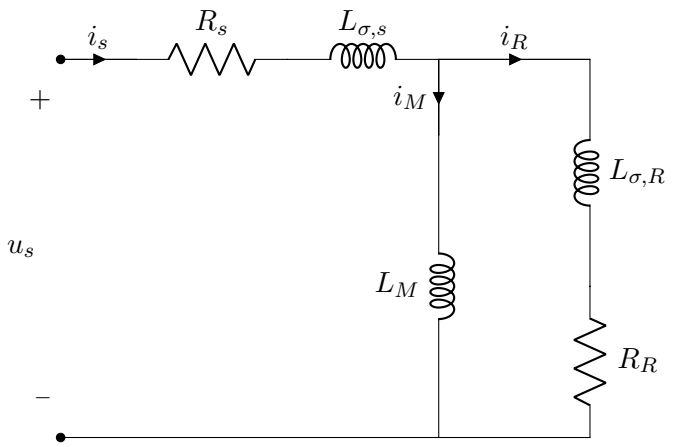

Figure 2.14: Per-Phase equivalent circuit of Induction motor

Using the transfer function of the equivalent circuit of figure 2.14 (equation 2.3), relying of the

hypothesis of $L_{\sigma,s} = L_{\sigma,R}$ and fixing the value of $\tau_\sigma = \frac{L_s+L_r}{R_r+R_s} = 9[ms]$ it was possible to estimate the motor parameters.
τ_σ is derived from the current waveform, as the initial rise of the current step response is determined by the total leakage inductance [12]. The estimated parameters, reported in the first row of table 2.4, are such that if we substitute them in 2.3 we obtain the same transfer function the System identification toolbox computed.

$$\frac{U(s)}{I(s)} = \frac{(L_s + L_M)s + R_R}{(L_s^2 + 2 \cdot L_s L_M)s^2 + (R_s(L_s + L_M)R_R(L_s + L_M))s + R_s R_R} \tag{2.3}$$

In the second row of the table are listed the parameters extracted from the FEM model, the description of the procedure is detailed in section 3.3.

	R_s	R_R	L_M	$L_{\sigma,s}$	$L_{\sigma,R}$
Signal Test	$1.1[\Omega]$	$0.62[\Omega]$	$121.8[mH]$	$7.7[mH]$	$7.7[mH]$
FEM extracted	$1.2[\Omega]$	$0.67[\Omega]$	$70.7[mH]$	$7.5[mH]$	$7.5[mH]$

Table 2.4: Estimated Machine Parameters (one phase)

The procedure followed is far from being a precise standstill self-commissioning one like the ones described in literature (for example [13]) and parameters computed in this way aren't very trustworthy, but this was the best viable option to get an idea of the real machine parameters.
One of the limits of this procedure is the uncertainty in the magnitude of τ_σ which affects the estimations of all the others parameters.
Anyway, as table 2.4 shows the values are not very far from the FEM extracted ones.

2.5 Stator rewinding

As mentioned in the introduction, the development of semiconductor devices allows inverters to withstand higher currents.
Being able to get more current triggered the increasing of power density of the induction machines used in railway traction([3] and [4]).
In particular [4] reveals a design strategy to improve the power density under the limit of outer diameter dimension, constraint that a motor for railway traction should respect.

The design change obviously has some implications in terms of losses as we discussed in the introduction.
Hoping to investigate this aspect from the experimental point of view, starting from three identical induction machines available in the laboratory, two of them were rewinded.

One of the machines has been rewinded doubling the section of the conductor and reducing by half the number of turns of the stator winding.
For the second one the ratio employed for reducing the number of turns and concurrently increasing the section of the conductor was 1.5.
Increasing of the section was obtained employing a bigger number of parallel wires per conductor.
Figure 2.15 shows the stator of a motor after the rewinding process.

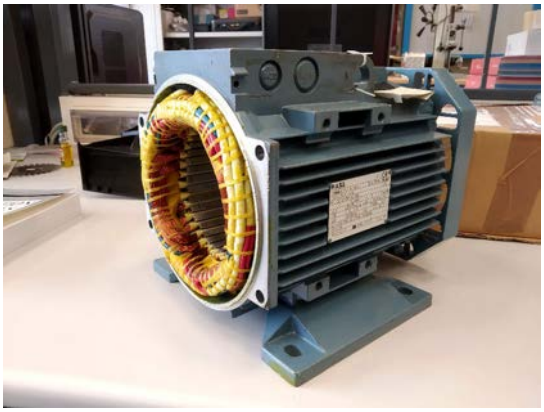

Figure 2.15: Rewinded Stator

3

Circuit models losses estimation

In this chapter the accuracy of different equivalent circuit models in predicting losses is tested. We will refer to the FEM analysis results as a benchmark.
Circuit parameters used in the analytical models are extracted from FEM simulations.
In the following sections are presented the two models that will be used, then the procedure used for parameters estimation is detailed.
Finally the performances predicted by the models are compared with the benchmark in three different stator voltage waveform scenarios: Sinusoidal, Six Step and SHE. This low frequency non-sinusoidal waveforms are the ones typically employed for feeding induction motors in the traction field.

3.1 Classic equivalent circuit machine model

The classic per phase equivalent circuit model is the simplest way to model an induction machine.
The well known circuit representation is reported in figure 3.1.
Figure 3.2 clarifies inputs and outputs quantities for this model.

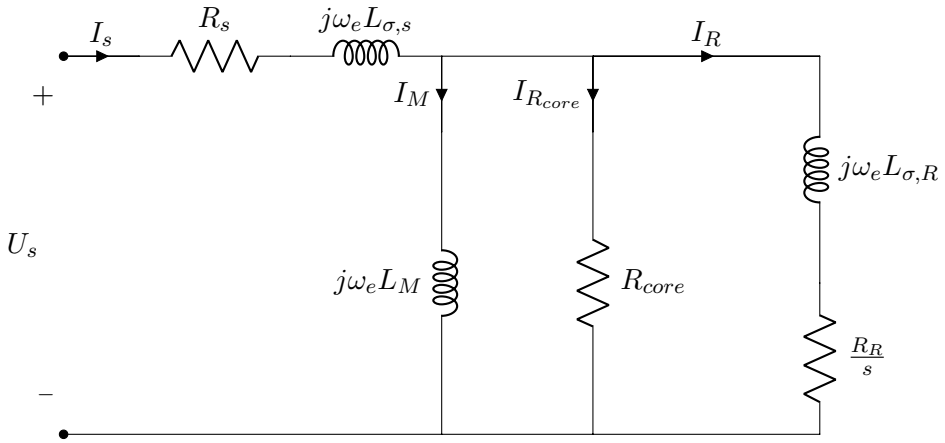

Figure 3.1: Per-Phase steady state equivalent circuit of Induction motor (considering core losses)

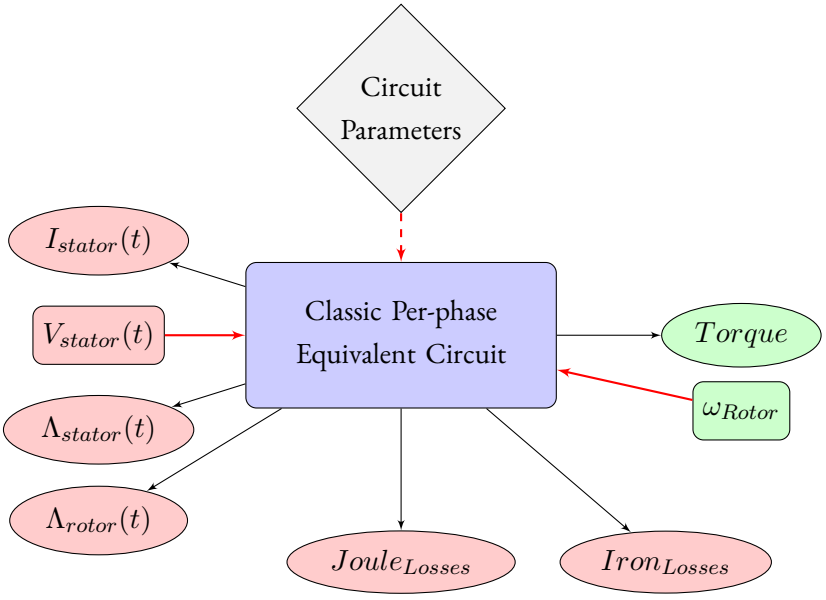

Figure 3.2: Classic equivalent circuit of induction machine block scheme

While the circuit reported in figure 3.1 is used to model the behaviour at the fundamental frequency, in order to estimate losses due to higher frequency harmonics the one reported in figure 3.3 was employed. The description of the algebraic manipulations used for getting that circuit are reported in appendix A.

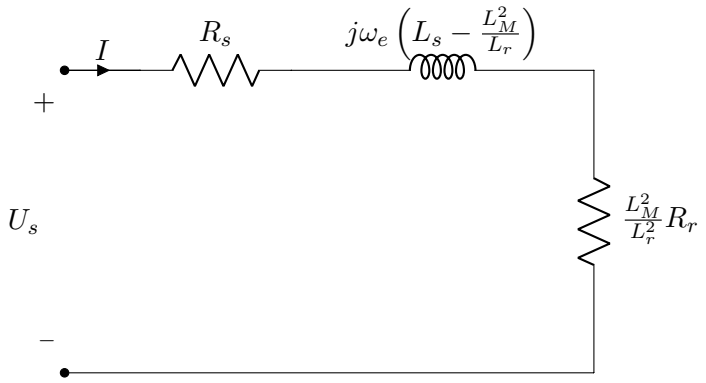

Figure 3.3: Per-Phase high frequency equivalent circuit of Induction motor

3.2 Core loss control machine model

Having available accurate models of the induction machine in the arbitrary $dq0$ reference frame plays a key role in its control.
In this models is common to ignore the core losses as they don't represent the majority of the machine's losses in full load operation but this is no longer true when the load decreases. Therefore a model which takes into account even the core losses is crucial for optimizing the operation of the machine in different load conditions and for better efficiency estimations in every operating point.

Such a model is derived in [5], and it's worth to underline its limit. This model works with high precision only for sinusoidal voltage excitation.
In the paper the accuracy of the model is tested for three different motor sizes, the comparison between model predictions and experimental measurements shows a 1% estimation error.

The mathematical derivation of the equations of the model starts from the classic three phase induction machine model that takes into account only copper losses (figure 3.4).

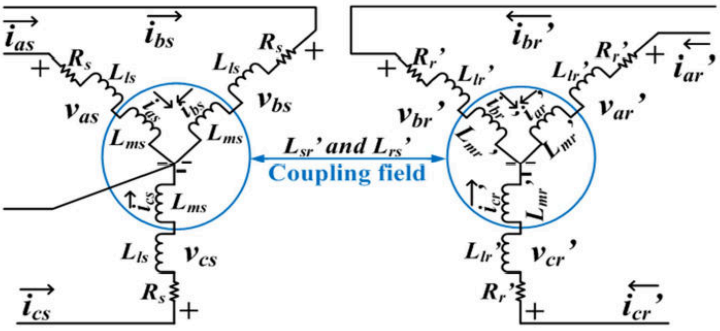

Figure 3.4: Classic three phase induction machine model (only copper losses)

Aiming at obtaining a model that can predict core losses even in transient conditions this representation has been modified putting a resistor in parallel to $L_{m,s}$ in each phase(figure 3.5).
Power lost in R_c corresponds to the core losses. This resistance value is not equal to the $R_{c,phase}$ used in the classic per phase equivalent circuit but in [5] it's proven that they are related.
Their correlation is described by equation 3.1.

$$R_c \approx \frac{2}{3} \cdot R_{c,phase} \tag{3.1}$$

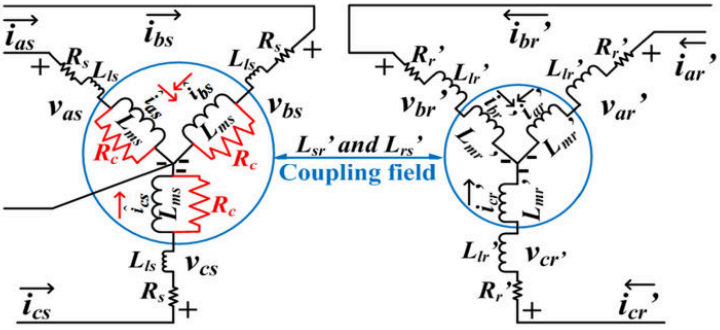

Figure 3.5: Three phase induction machine model (copper and core losses)

For both stator and rotor it is possible to write voltage, current and flux equations. By applying the *abc* to *dq*0 transformation we can express those equations in an arbitrary reference frame rotating at an angular speed ω.
This manipulation leads to equations 3.2 to 3.17 and the equivalent circuits of figure 3.6.

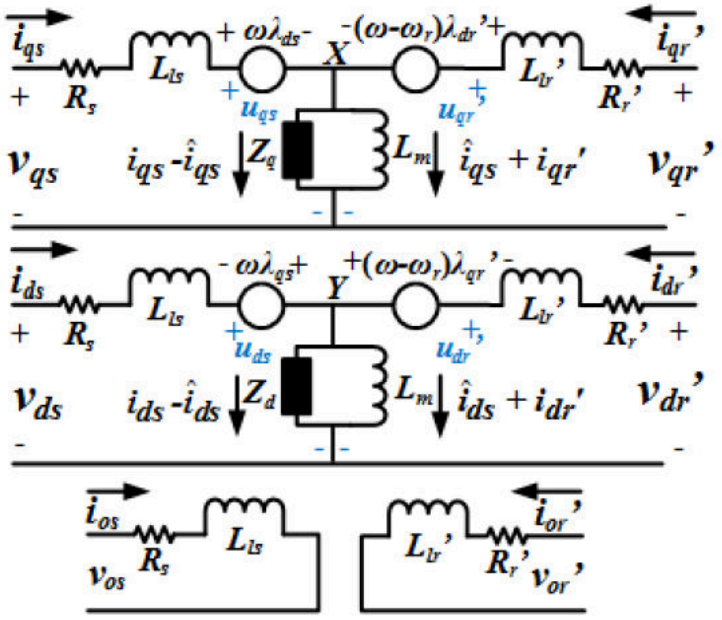

Figure 3.6: Induction machine model in arbitrary reference frame (copper and core losses)

$$v_{qs} = R_s i_{qs} + \omega\lambda_{ds} + \frac{d(\lambda_{qs})}{dt} \tag{3.2}$$

$$v_{ds} = R_s i_{ds} - \omega\lambda_{qs} + \frac{d(\lambda_{ds})}{dt} \tag{3.3}$$

$$v'_{qr} = R'_r i'_{qr} + (\omega - \omega_r)\lambda'_{dr} + \frac{d(\lambda'_{qr})}{dt} \tag{3.4}$$

$$v'_{dr} = R'_r i'_{dr} - (\omega - \omega_r)\lambda'_{qr} + \frac{d(\lambda'_{dr})}{dt} \tag{3.5}$$

$$i_{qs} = \hat{i_{qs}} + \frac{L_{ms}}{R_c}\omega\hat{i_{ds}} + \frac{L_{ms}}{R_c}\frac{d(\hat{i_{qs}})}{dt} \tag{3.6}$$

$$i_{ds} = \hat{i_{ds}} - \frac{L_{ms}}{R_c}\omega\hat{i_{qs}} + \frac{L_{ms}}{R_c}\frac{d(\hat{i_{ds}})}{dt} \tag{3.7}$$

$$\lambda_{qs} = L_{ls} i_{qs} + L_m(\hat{i_{qs}} + i'_{qr}) \tag{3.8}$$

$$\lambda_{ds} = L_{ls} i_{ds} + L_m (\hat{i_{ds}} + i'_{dr}) \tag{3.9}$$

$$\lambda'_{qr} = L'_{lr} i'_{qr} + L_m (\hat{i_{qs}} + i'_{qr}) \tag{3.10}$$

$$\lambda'_{dr} = L'_{lr} i'_{dr} + L_m (\hat{i_{ds}} + i'_{dr}) \tag{3.11}$$

$$v_{0s} = R_s i_{0s} + \frac{d(\lambda_{0s})}{dt} \tag{3.12}$$

$$v'_{0r} = R'_r i'_{0r} + \frac{d(\lambda'_{0s})}{dt} \tag{3.13}$$

$$i_{0s} = \hat{i_{0s}} + \frac{L_{ms}}{R_c} \frac{d(\hat{i_{0s}})}{dt} \tag{3.14}$$

$$\lambda_{0s} = L_{ls} \hat{i_{0s}} \tag{3.15}$$

$$\lambda'_{0r} = L'_{lr} i'_{0r} \tag{3.16}$$

$$\omega_r = p \cdot \omega_{r,mec} \tag{3.17}$$

Joule losses are trivially given by 3.18, while some algebraic manipulations are required to get the expression for the core losses.
The one reported in 3.19 it's true only if the $dq0$ frame is synchronous with the rotor (alignment between rotor flux and d axis is not necessary).

$$P_{cu} = \frac{3}{2} \left[R_s (i_{qs}^2 + i_{ds}^2) + R'_r (i'^2_{qr} + i'^2_{dr}) \right] \tag{3.18}$$

$$P_{fe} = \frac{3}{2} \frac{\omega_e^2 L_m L_{ms}}{R_c} \left(\hat{i_{ds}}^2 + \hat{i_{ds}} i'_{dr} + \hat{i_{qs}}^2 + \hat{i_{qs}} i'_{qr} \right) \tag{3.19}$$

3.2.1 Implementation

The $dq0$ model of the machine with core losses was then implemented in a dynamic simulation software by means of the equations listed in the previous section(3.2 to 3.19).
An immediate visualisation of the input and outputs is given by figure 3.7.

The three stator voltages and the rotor speed are the inputs of the model as well as the circuit parameters employed in the equations.

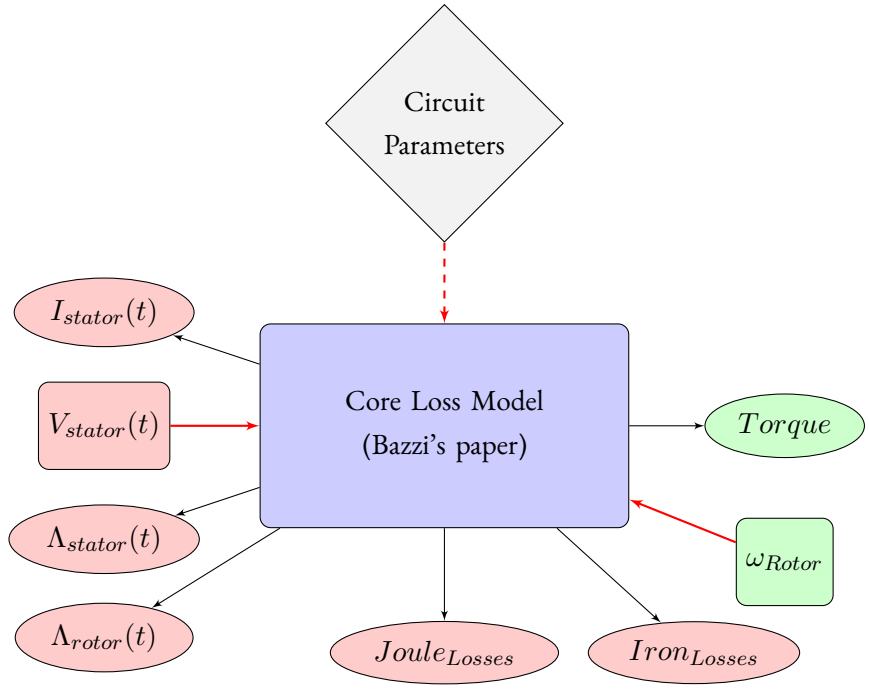

Figure 3.7: Bazzi's core loss model block diagram

In the example reported in [5] the imposed quantity, besides the stator voltages, is the load torque.
In our case the load torque is defined to have a magnitude such that the motor's slip equals the desired one.
The difference between the desired rotor speed and the actual one is the error entering the *PID* controller whose output is the load torque. Rotor speed is generated with the well known dynamic which involves inertia, load and electromagnetic torque (as we are not considering air friction).
For better comprehension the block diagram is reported in figure 3.8.

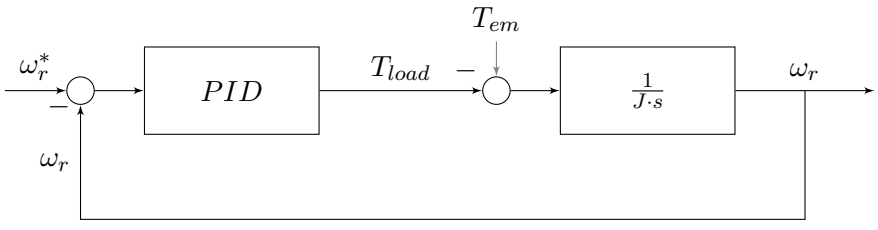

Figure 3.8: Rotor speed controller

3.3 Parameters estimation

As we mentioned earlier, the parameters used in these models were extracted from the finite elements model.
This was necessary because employing the ones estimated by RMxprt lead to a mismatch between the analytical models results and the finite element ones. Mismatch that reduced when relying on the FEM model extracted parameters.
The interest was in getting the values of: stator and rotor resistance, stator and rotor leakage inductance, mutual inductance and core loss resistance.
The stator resistance is immediately given by the software, it is estimated starting from the winding specifications and material taking into account the end winding resistance too.
A couple of test were necessary to estimate the other quantities, keeping in mind that the software already considers the end winding effects, in terms of resistance and leakage reactance, for the stator winding and for the rotor cage as well, as we mentioned earlier in section 2.2 .
We hypothesized that stator and rotor leakage reactances were equal.

Locked rotor test At first was performed a locked rotor test with magnitude of voltage reduced to the 25% of the nominal value in order to get a current amplitude close to the nominal one.
In this operating condition the equivalent circuit of the induction machine is the one represented in figure 3.9.

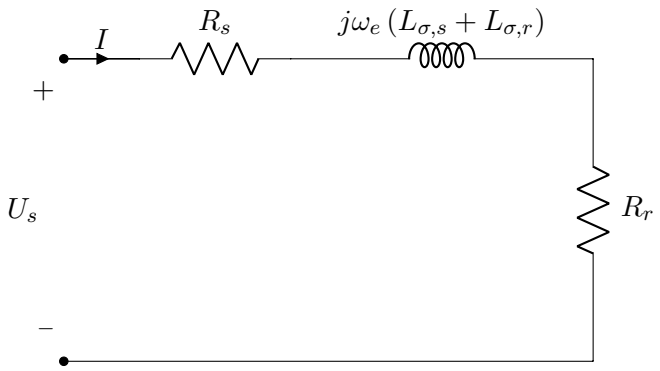

Figure 3.9: Circuit model in locked rotor condition

Relying on the FEM results and on the model of figure 3.9 we managed to compute the values of R_r and $L_{\sigma,r} = L_{\sigma,s}$.
Knowing the total power absorbed by the machine we evaluated the power factor:

$$cos(\phi_{LR}) = \frac{P_{1phase}}{U_s \cdot I}$$

Then we calculated the equivalent impedance.
Its real and imaginary parts allowed, knowing the stator resistance and assuming the stator and rotor leakage reactances to be equal, the determination of the parameters of interest.

$$Z_{LR} = |R_s + R_r + j\omega_e \left(L_{\sigma,s} + L_{\sigma,r}\right)| = \frac{U_s}{I}$$

$$R_r = Z_{LR} \cdot cos(\phi_{LR}) - R_s$$

$$L_{\sigma,r} = L_{\sigma,s} = \frac{Z_{LR} \cdot sin(\phi_{LR})}{2\pi f}$$

Figures 3.10 and 3.11 are the induction magnitude and flux line maps in locked rotor operation.

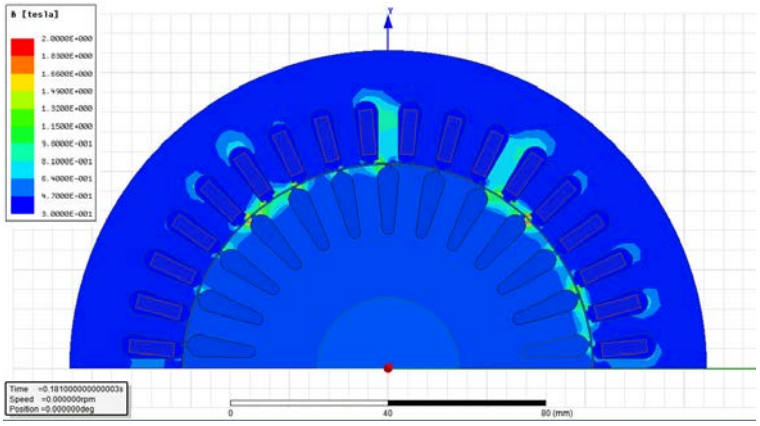

Figure 3.10: Magnitude of $\boldsymbol{B}$ vector in locked rotor condition

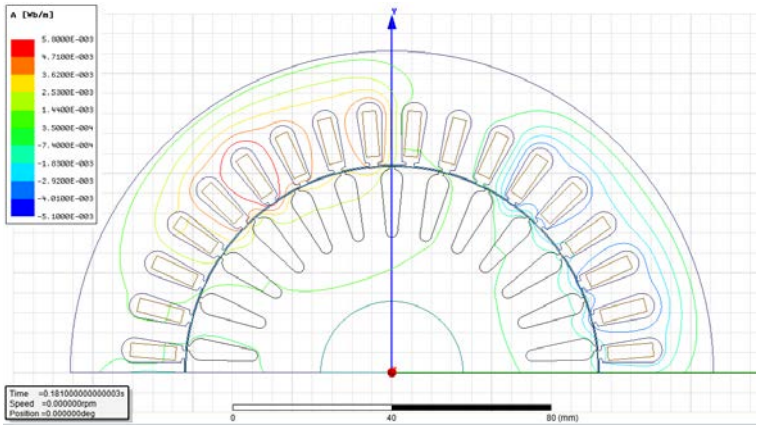

Figure 3.11: Flux lines in locked rotor condition

NO LOAD TEST The no load test was performed at nominal voltage condition and imposing the rotor speed to be equal to the synchronous one.
In order to compute the parameters in this circumstance we based ourselves on the equivalent circuit of figure 3.12

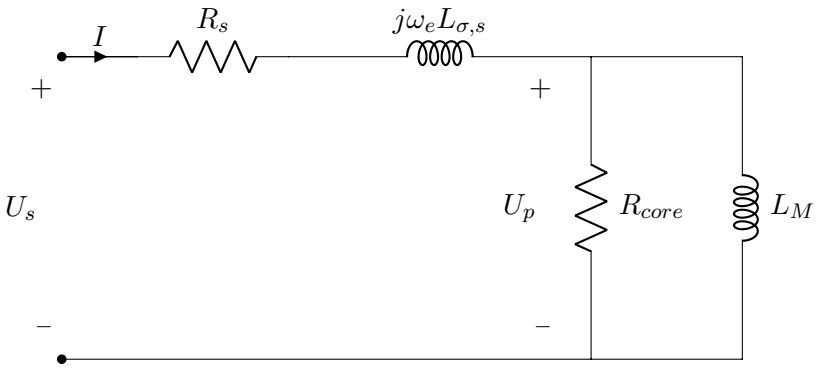

Figure 3.12: Circuit model in no load condition

In a similar fashion to what did for the no load test we post-processed the FEM analysis results to calculate the ϕ_{NL}.

$$cos(\phi_{NL}) = \frac{P_{1phase}}{U_s \cdot I}$$

Then it was possible to estimate R_{core} and L_M proceeding as follows:

$$\underline{U_p} = U_s - (R_s + j\omega L_{\sigma,s}) \cdot Ie^{-j\phi_{NL}}$$

$$\underline{Y_p} = \frac{\underline{I}}{\underline{U_p}} = \left(\frac{1}{R_{core}} + \frac{1}{j\omega L_M}\right)^{-1}$$

$$R_{core} = \frac{1}{\Re\left(\underline{Y_p}\right)}$$

$$L_M = -\frac{1}{\Im\left(\underline{Y_p}\right) \cdot \omega}$$

Figures 3.13 and 3.14 show the induction magnitude and flux line maps in no load operation.

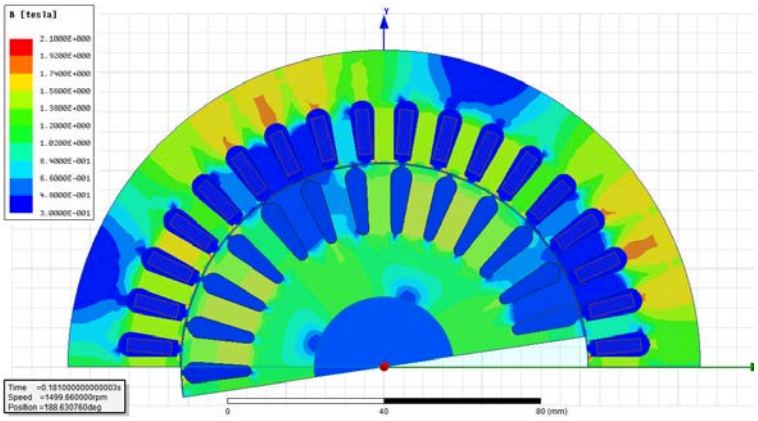

Figure 3.13: Magnitude of $\boldsymbol{B}$ vector in no load condition

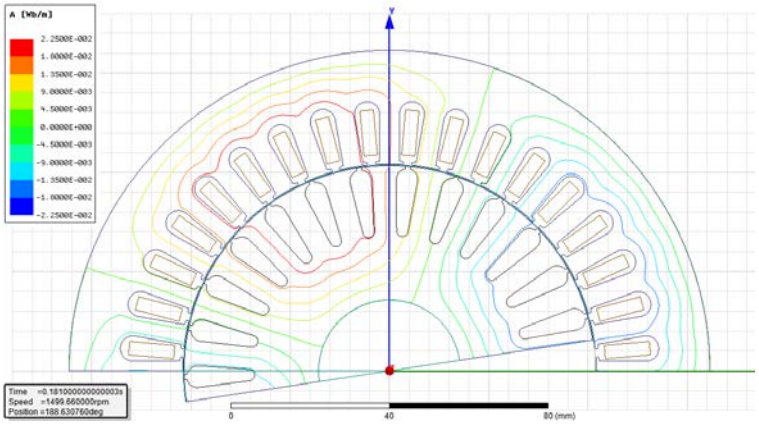

Figure 3.14: Flux lines in no load condition

The parameters' values are finally reported in table 3.1.

L_M	$L_{\sigma,s}$	$L_{\sigma,r}$	R_{core}	R_s	R_r
$70.7[mH]$	$7.5[mH]$	$7.5[mH]$	$1576[\Omega]$	$1.2[\Omega]$	$0.67[\Omega]$

Table 3.1: Circuit parameters estracted from the FEM model

3.4 Models prediction comparison

The estimations comparison of copper losses, core losses and torque carried out by the FEM and the two analytical models are presented in this section.
In each voltage scenario the rotor speed has been fixed to $1462[rpm]$. The magnitude of the voltage in the sinusoidal case is equal to the nominal one.
Concerning the non-sinusoidal cases explored we used a six step waveform, figure 3.15, and a SHE one, figure 3.16, aiming at eliminating the fifth harmonic.
In both cases the waveforms present a fundamental whose magnitude is equal to the nominal voltage.

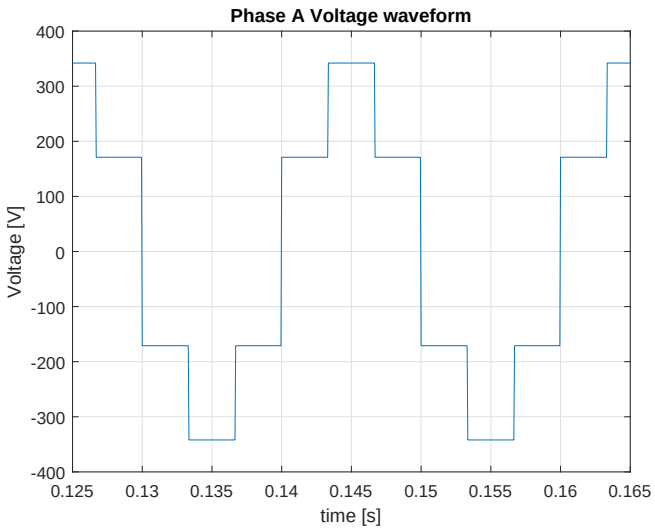

Figure 3.15: Phase A Voltage Six Step excitation

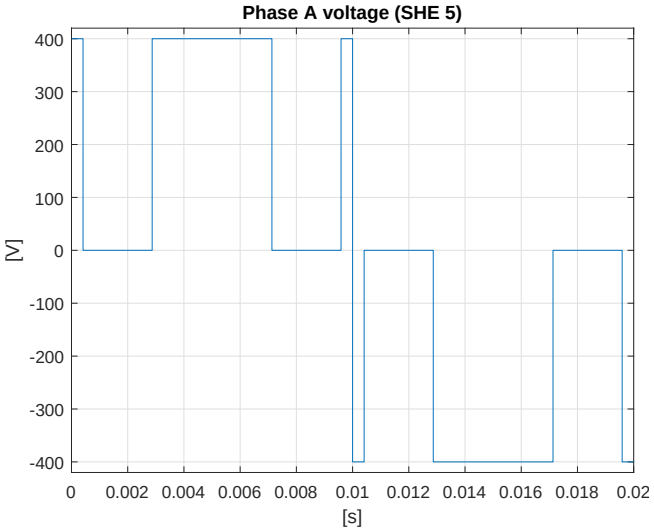

Figure 3.16: Phase A voltage waveform (Selective Harmonic elimination of fifth harmonic)

A detailed description of SHE can be found in [14] and [15]. Here we just want to provide some basic informations.
In this modulation scenario the number of commutation angles per quarter period is fixed in advance. Selective harmonic elimination is employed in high power applications where a trade off between switching losses in the power electronic components and disturbances introduced by the low switching frequency has to be made.
In our case the waveform is produced by a three level inverter and the number of switching angles per quarter period is 2.
Each switching angle gives one degree of freedom, two angles allow us, for example, to: set the amplitude of the fundamental and eliminate the fifth harmonic of voltage. Another possibility could be, instead of eliminating the fifth harmonic, minimizing the fifth and the seventh.
Equation 3.20 gives the magnitude of the $n-th$ harmonic in our scenario: 2 switching angles(α_1 and α_2 with $\alpha_1 < \alpha_2$), starting connected to the positive(or negative rail of the $DC-link$) and clamped to zero in between α_1 and α_2.

$$|V_n| = \frac{4E}{n\pi}\left(1 - cos(n\alpha_1) + cos(n\alpha_2)\right) \tag{3.20}$$

This means that the angles desired to satisfy our requirements are α_1 and α_2 such that they are solution of 3.21 and 3.22.

$$|V_1| = \frac{4E}{\pi}\left(1 - cos(\alpha_1) + cos(\alpha_2)\right) \tag{3.21}$$

$$0 = \frac{4E}{5\pi}\left(1 - cos(5\alpha_1) + cos(5\alpha_2)\right) \tag{3.22}$$

Bar graphs presenting losses and torque comparisons are reported in figures 3.17, 3.18 and 3.19.

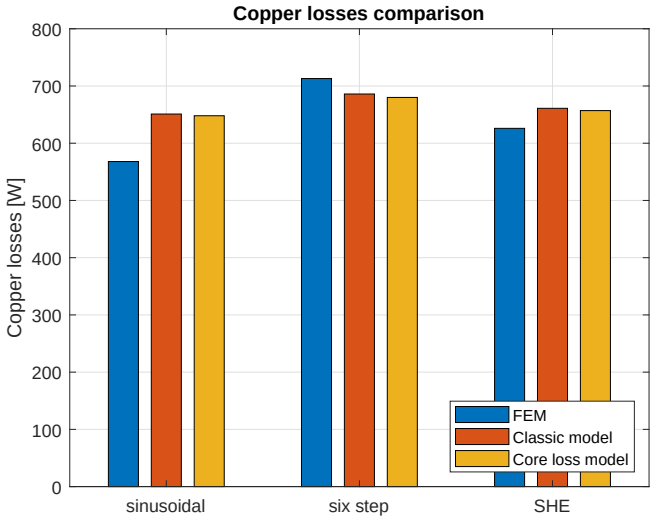

Figure 3.17: Copper losses estimation in three different voltage scenarios (FEM vs analytical models)

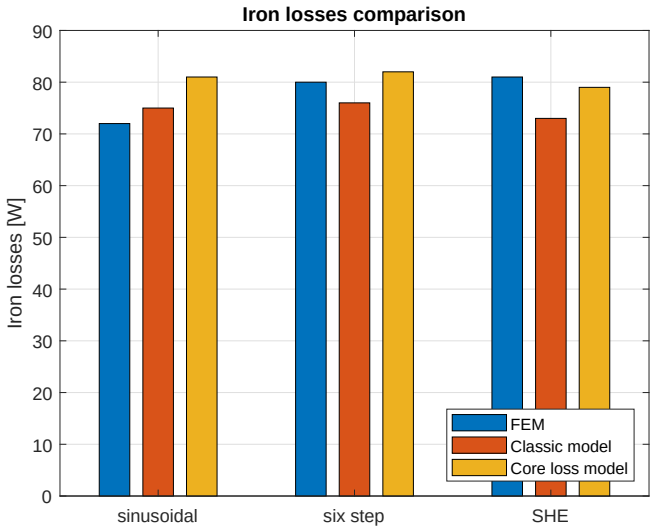

Figure 3.18: Iron losses estimation in three different voltage scenarios (FEM vs analytical models)

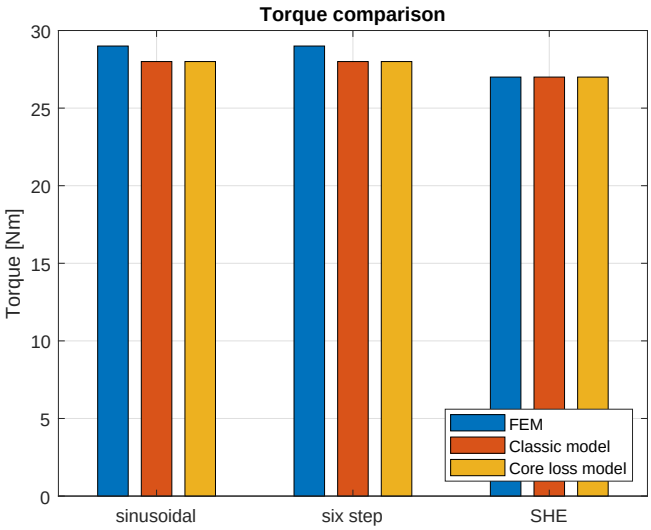

Figure 3.19: Torque estimation in three different voltage scenarios (FEM vs analytical models)

Both cases involving non sinusoidal excitation exhibit an underestimation of the core losses by the analytical model, while in the sinusoidal voltage scenario they overestimated them.
This happens because of the circuit employed for modelling the motor behaviour at high frequency (figure 3.3), as there is no core loss resistance it doesn't take into account this kind of losses.
Furthermore the analytical model doesn't consider the so called *stray load losses* (SLL). Those include all the loss mechanism that the lumped circuit parameters does not describe for example: The non-sinusoidal spatial *magneto motive force* (MMF) wave that is responsible of non-modelled currents, and therefore losses in the rotor; or the harmonics of the air gap flux density, responsible of increased core losses ([16]).

Superposed upon the current and forces due to the fundamental field of an induction machine, there are many smaller currents and forces produced by the miriad of harmonics fields that are present - just as every ocean wave is surmounted by many ripples. [17]

Philip L. Alger

4

Estimation of torque ripple due to current harmonics

In this section, after providing a brief theoretical explication of torque harmonics generation, we compare the results provided by FEM and dynamic simulation post-processing computations in order to check the reliability of torque pulsations estimation carried out with a simple *dq* machine model.
Transient simulations were run in the FEM software. Stator voltages and rotor speed are the imposed quantities and, as we did before, three different voltage scenarios were investigated. Imposed voltages and the consequent currents feed the flux observer post-processing model.
Torque computed by FEM analysis and estimated by the flux observer were then post-processed.
Fast Fourier transform (FFT) was performed and harmonic magnitudes and frequencies compared in a bar graph. The spectrum of voltages and currents for each excitation type is shown too.
In the last section the accuracy of low frequency torque harmonics prediction using current ones is confirmed by operating a torque spectrum ”cleaning” via q-axis current harmonics.

In order to get a clear understanding of the inputs and outputs quantities for the different models is useful to observe the flow charts 4.1 and 4.2.
Inputs are represented with a rectangular block and red arrows, outputs present elliptic blocks and black arrows.
Electromagnetic quantities have red background colour while green background characterizes mechanical ones.

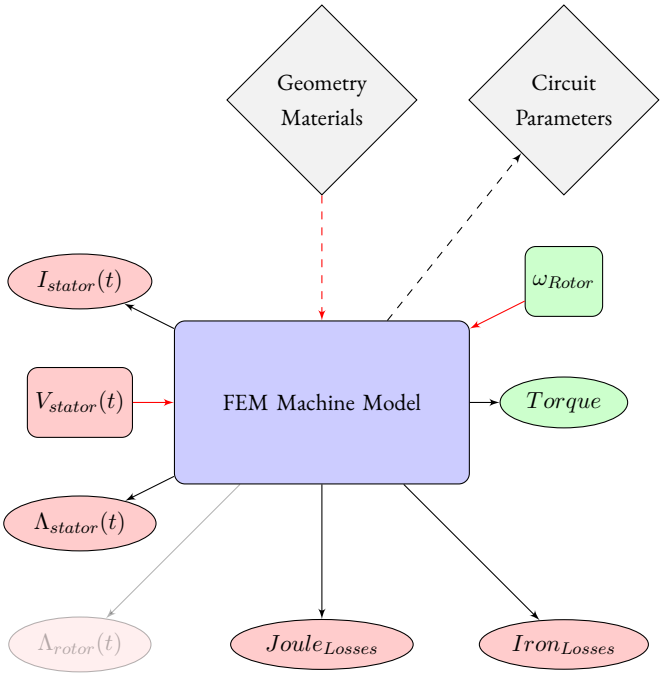

Figure 4.1: FEM model block diagram

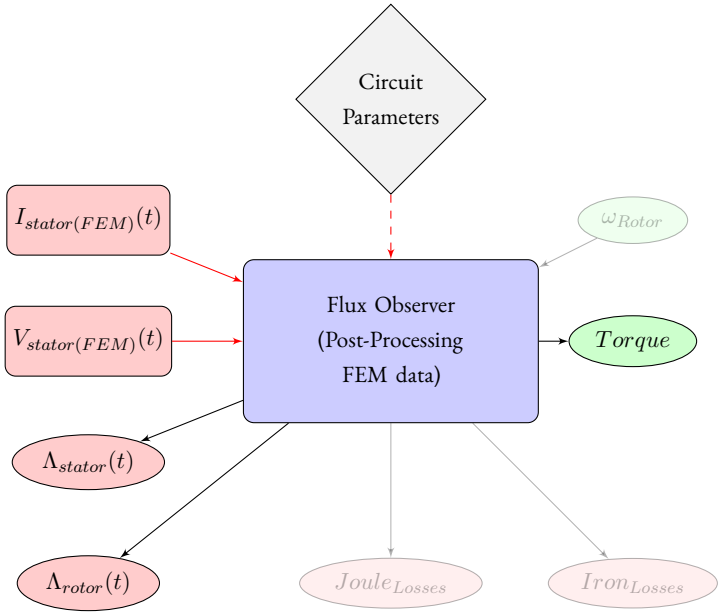

Figure 4.2: Flux Observer block diagram

The flux observer model doesn't compute the high frequency torque harmonics due to slotting, but does compute the ones due to current harmonics and those ones exhibit a good match with

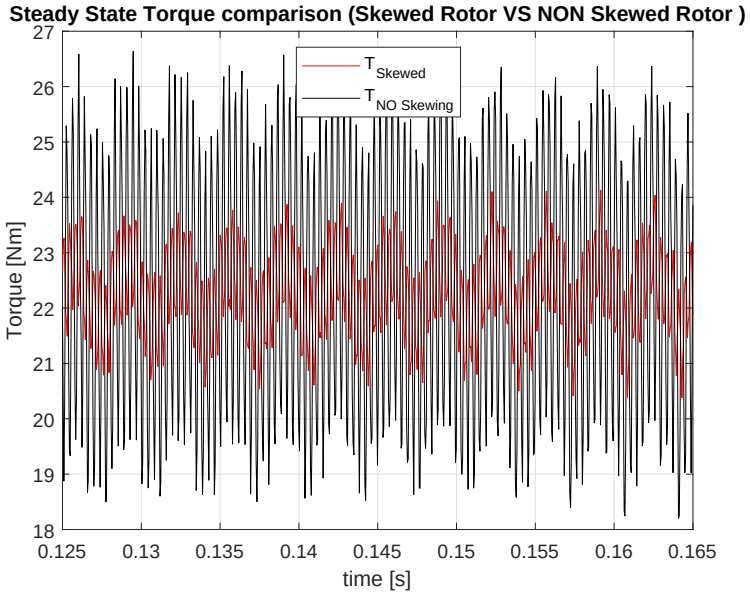

Figure 4.3: Skewing effect on steady state Torque

FEM results.

Torque harmonics due to slotting can appear at high frequencies that depend on the number of stator slots, rotor bars, electrical frequency, slip and number of pole pairs [18], [19].

By considering the Skew model the software is able to mitigate those harmonics as it emerges from the comparison of the results concerning two simulations run with sinusoidal voltage excitation. One employs the skewing model while the other doesn't (figures 4.3 and 4.4).

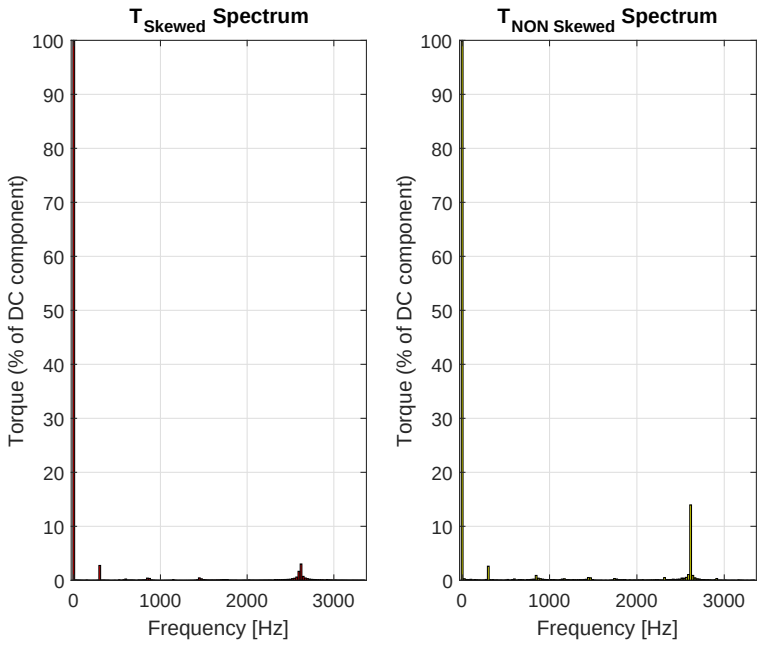

Figure 4.4: Skewing effect on Torque Spectrum

4.1 Torque harmonics generation

By taking a look to current and torque spectra (for example figures 4.9 and 4.8) is easy to notice that low frequency torque harmonics appear at the same frequencies of the current ones (if they are represented in a synchronous reference frame).
In this case the fundamental is located at $0[Hz]$, the fifth harmonic at $-6f_{fundamental}$, the seventh harmonic at $6f_{fundamental}$, etc.
It is worth spending some words describing how these harmonics are generated.

A set of three phase currents flowing through the stator winding of an induction machine produces a time varying spatial distribution of magneto motive force along the air gap. If we consider only the fundamental we get a sinusoidal spatial distribution of MMF rotating at a precise angular speed, the synchronous speed, given by the well known 4.1.

$$\omega_{e,1} = p \cdot \omega_{m,1} = 60 \cdot f_1 \, [rpm_{el}] \tag{4.1}$$

The flux density associated to this wave is commonly addressed as the rotating magnetic field.

Supposing to feed the motor with a voltage waveform that is not sinusoidal, for example the classic six step wave, voltages and therefore currents will present a certain harmonic content.

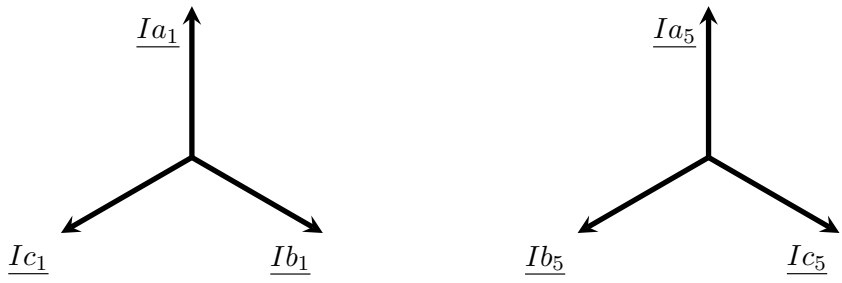

(a) Direct sequence triad

(b) Inverse sequence triad

Figure 4.5: Fundamental and fifth harmonic currents

Each one of the harmonic components of the current, flowing through the three phase stator winding will produce a rotating magnetic field. As we will detail later those fields will present different magnitude and differ as well in the magnitudes and signs of rotating speeds associated with each one of them.

Speed differences are a consequence of the fact that rotating fields are produced by currents at different frequencies(4.1).
The direction of rotation differs because of the different phase shift that exists between phase current harmonics of different order.

As an example, for the fundamental currents:

$$\angle \underline{Ib_1} - \angle \underline{Ia_1} = 120^\circ$$

While for the fifth harmonic:

$$\angle \underline{Ib_5} - \angle \underline{Ia_5} = 240^\circ$$

With this kind of computations it's easy to prove that the fundamental currents, and all the harmonics with order $h = 6k + 1$ (where $k = 1, 2, 3, ...$), form a direct triad while the fifth harmonic currents, and all the harmonics with order $h = 6k - 1$ from an inverse one(4.5).

The rotating field produced by the inverse triads harmonics rotates in the opposite sense respect to the fundamental one.
In order to summarize what has just been stated an example of the rotating field generated by the fundamental, the fifth and the seventh harmonic is represented in figure 4.6.

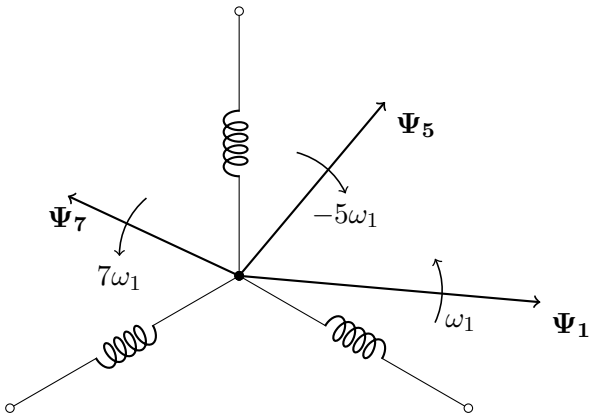

Figure 4.6: Fundamental and harmonic fields

Each rotating harmonic field that links rotor conductors induce a voltage and therefore a current in the rotor circuit. The frequency of these induced quantities will depend on the relative speed among the field and the rotor. Each one of the rotor's harmonic current will produce a rotating field as well. Independently of the rotor speed this field will be rotating synchronously to the same order stator harmonic field.

In this context we can consider torque to be produced as an interaction between stator and rotor rotating magnetic fields, and to be proportional to the magnitude of these fields and the sine of the angle between them.
Form the previous consideration follows the fact that steady torque will be produced only by synchronous rotating fields.
The only relevant steady torque is generated by the fundamental fields, same order harmonic ones don't contribute significantly to torque, their interaction can be neglected.
If we consider as an example the fundamental stator field and the fifth harmonic rotor one, the sine of the angle between them will keep varying as they are not synchronous. This leads to a torque with zero mean value pulsating at a frequency equal to the frequency corresponding to the relative speed between the two different harmonic vectors.
Due to the high inertia of the motor the speed is dictated by the steady torque, while pulsating torque doesn't usually imply speed pulsations.
At this point is important to underline that a reference frame synchronous with the fundamental rotating field, in other words rotating at ω_1 (see figure 4.6), sees the fifth and seventh harmonic fields rotating at the same speed, in absolute value, but with opposite signs($\pm 6\omega_1$).

So the interactions between fundamental stator field with fifth harmonic rotor field and seventh

harmonic one, both generate a torque pulsating at the same frequency.
This two isofrequentially pulsating torques will compose to generate the sixth harmonic of the torque waveform.

4.2 Sinusoidal Voltage

The first simulation is done in nominal conditions. Sinusoidal voltage is imposed to the stator windings and rotor speed is set to be equal to the rated value $1462[rpm]$.
In 4.7 the steady state waveform of torque computed by means of FEM analysis and estimated by the flux observer is shown.
Here is possible to appreciate what was mentioned before, there's a good matching in the low frequency ripple while this is not true for the higher frequencies harmonics due to the slotting effects. They appear with a greater magnitude in the torque waveform computed by the finite element simulation.
Spectra of current and voltage spatial vectors are shown in 4.8, in the $\alpha\beta$ stationary reference frame.
In figure 4.9 comparison of torque harmonics computed by the two methods is presented, the magnitude of every harmonic is scaled in percentage to the DC component of the finite element simulation computed torque.

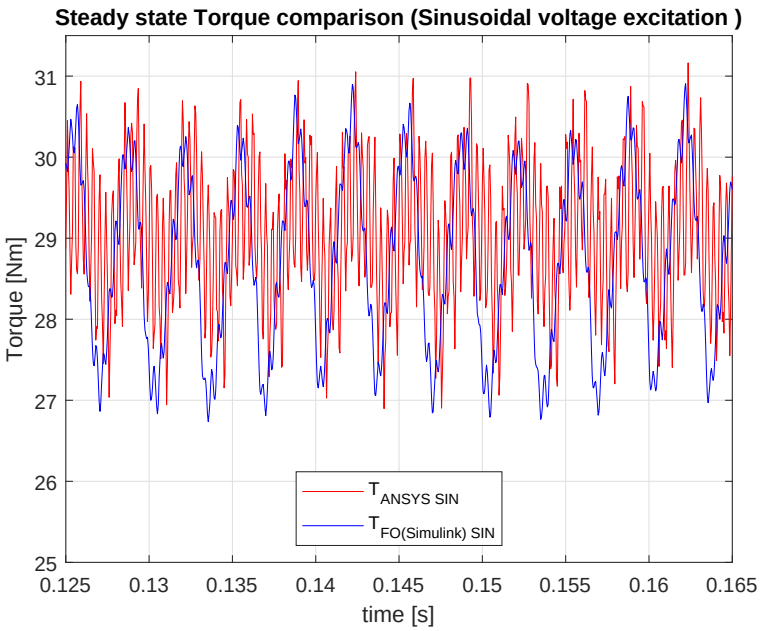

Figure 4.7: Sinusoidal excitation steady state Torque (FEM vs Flux observer post-processing)

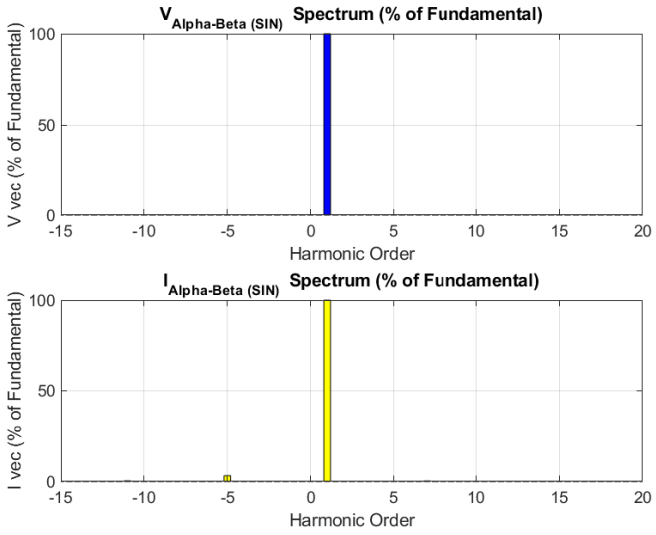

Figure 4.8: Spectrum of voltage and current spatial vectors (Stationary reference frame)

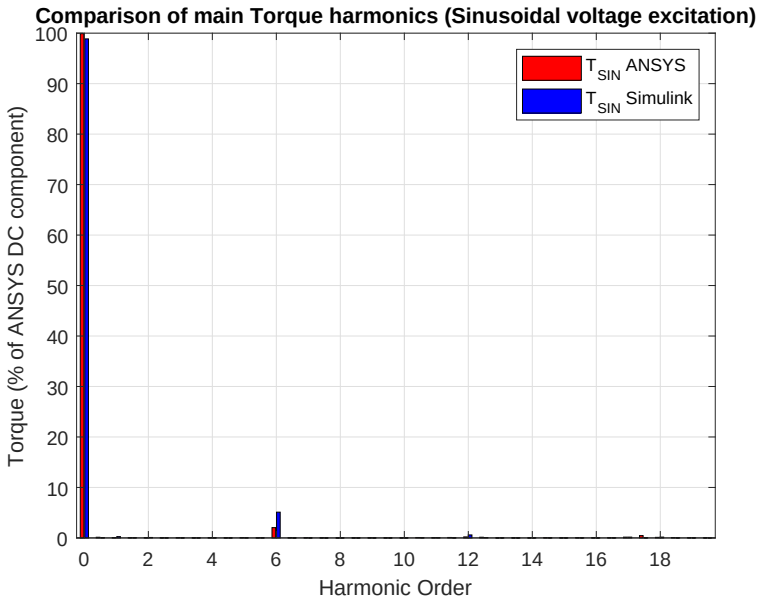

Figure 4.9: Torque Harmonics FEM vs Flux observer post-processing estimation

For the sake of completeness the no load simulation was performed too.
Even in this case the prediction of torque by the flux observer is precise. This is confirmed by figure 4.10.

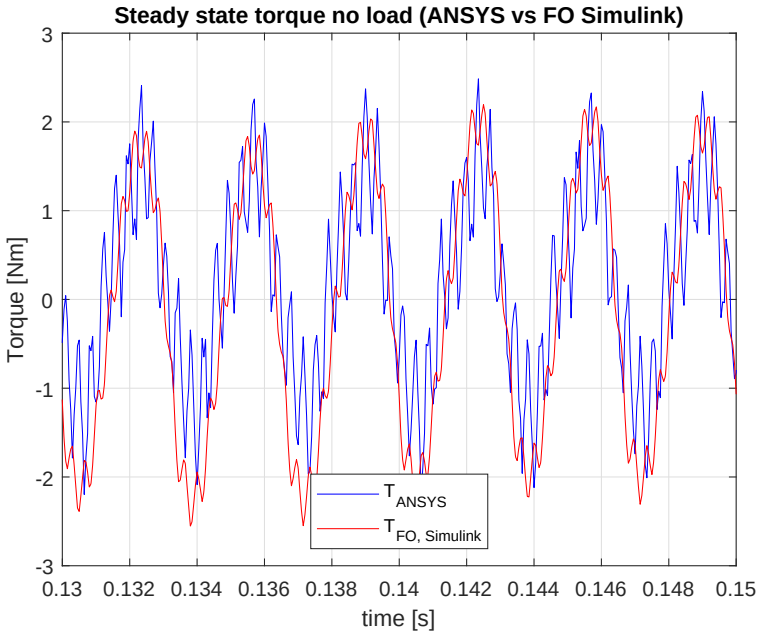

Figure 4.10: Sinusoidal excitation no load steady state Torque (FEM vs Flux observer post-processing)

4.3 Six Step Voltage

This simulation is run imposing a Six Step voltage wave to the stator winding (figure 4.11) at the rated rotor speed ($1462[rpm]$), the amplitude of the six step wave is set so that the magnitude of its fundamental harmonic equals the rated voltage of the motor.
From looking at the torque waveform in figure 4.12 we get another confirmation of the good estimation of the low frequency torque ripple. Another chance to check this is provided by the spectra comparison in figure 4.14.

It is possible to notice (figures 4.13 and 4.12) how dominant current harmonics, in other words the ones with higher amplitude (the fifth and the seventh), both concur to generate the biggest torque harmonic. This happens because the interaction between the fundamental of the flux and a current harmonic, which has different frequency respect to the fundamental flux one, produces a pulsating torque whose frequency depends on the relative frequency between flux fundamental and current harmonic.
As is known from theory and confirmed in figure 4.13, fifth harmonic of the current vector is counter-rotating with a frequency $-5f_{fundamental}$ and the seventh is rotating in the same direction as the fundamental with frequency $7f_{fundamental}$.
So the relative speed between the flux vector fundamental, synchronous with the current vector

fundamental, and the fifth harmonic of current is $-6f_{fundamental}$, while if we consider the seventh is $6f_{fundamental}$. That produces two pulsating torques at the same frequency, with zero DC component, that compose to build the sixth harmonic of torque, the biggest harmonic in figure 4.14.

The good matching between the results implies a good reliability of the parameters extracted as described in the previous chapter.

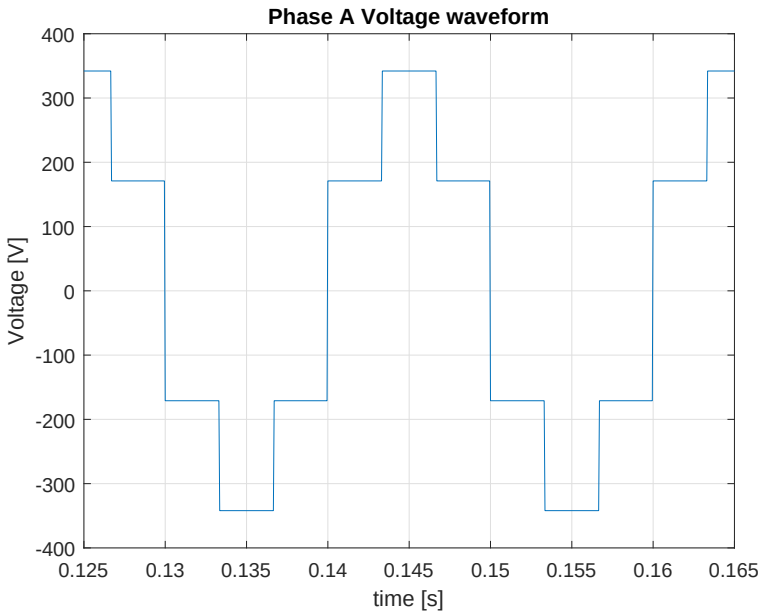

Figure 4.11: Phase A Voltage Six Step excitation

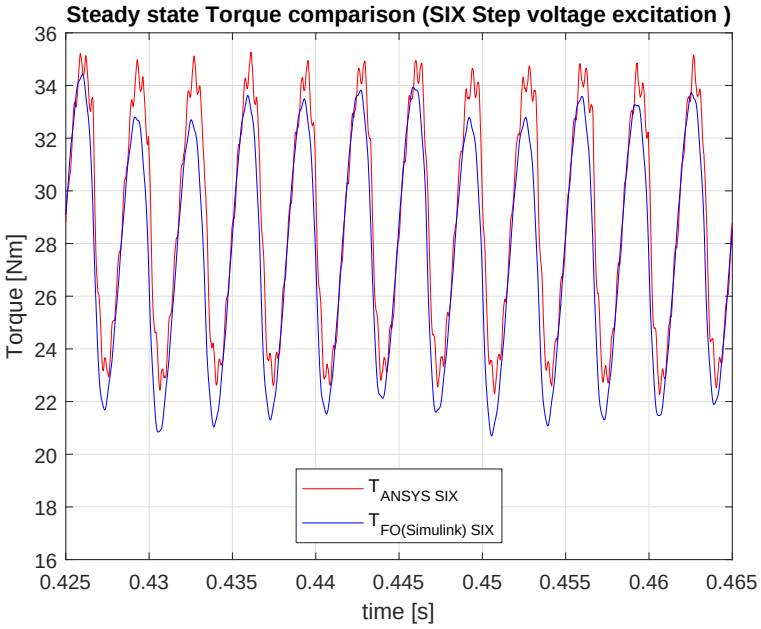

Figure 4.12: Six Step steady state Torque (FEM vs Flux observer post-processing)

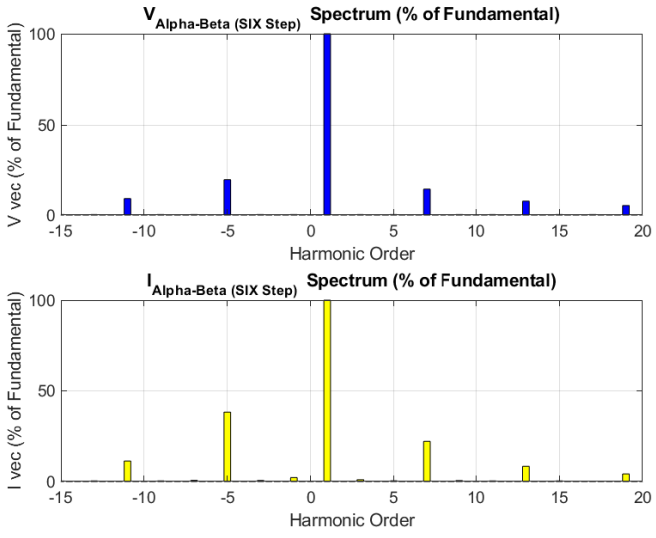

Figure 4.13: Spectrum of voltage and current spatial vectors (Stationary reference frame)

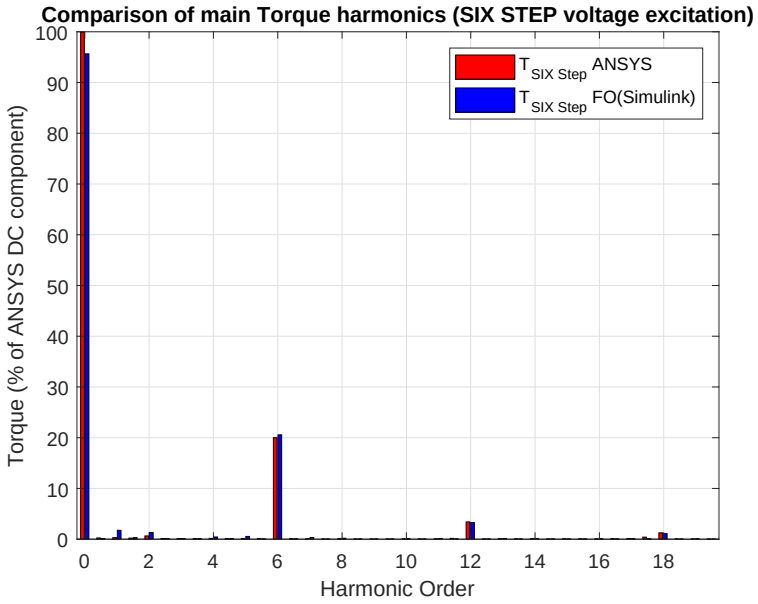

Figure 4.14: Torque Spectrum (FEM vs Flux observer post-processing)

Now it is important to clarify that even though the torque waveform with sinusoidal excitation seems more distorted than the one corresponding to the six step scenario that is not true as it is shown in figure 4.15. It seems to be like that but the low frequency oscillation is ten times bigger in the six step case and this hides the high frequency one making it look smaller.

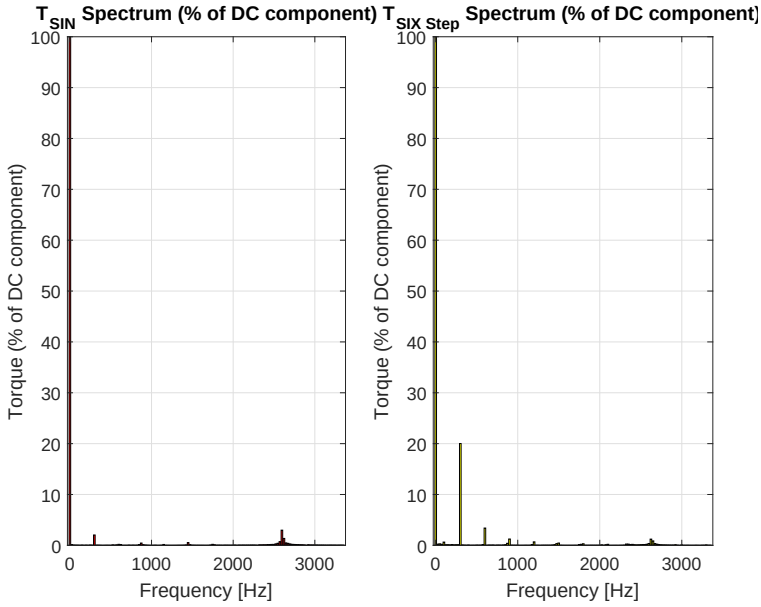

Figure 4.15: Spectrum of torque in sinusoidal and six step excitation

4.4 Selective Harmonic elimination

Another simulation was run by feeding the motor with a voltage waveform that implements Selective Harmonic Elimination (*SHE*).
It employs two switching angles per quarter period, this means that there are two degrees of freedom so that is possible, for example, to impose the fundamental voltage magnitude and eliminate one specific harmonic, or to impose the fundamental voltage magnitude and mitigate the magnitude of a certain group of harmonics.
In this case the switching angles were chosen aiming at imposing the amplitude of the fundamental and eliminating the fifth harmonic of the current.

Let E be the maximum voltage value that the three level inverter can provide (the DC link voltage), then the fundamental magnitude is given by 4.2.

$$\hat{V}_{fundamental} = 0.8 \cdot E \tag{4.2}$$

For this simulation was chosen a value of $E = 400[V]$ that causes the fundamental to be very close the rated machine voltage $\hat{V}_{fundamental} = 320[V]$.
One period of the phase A voltage is reported in figure 4.16.

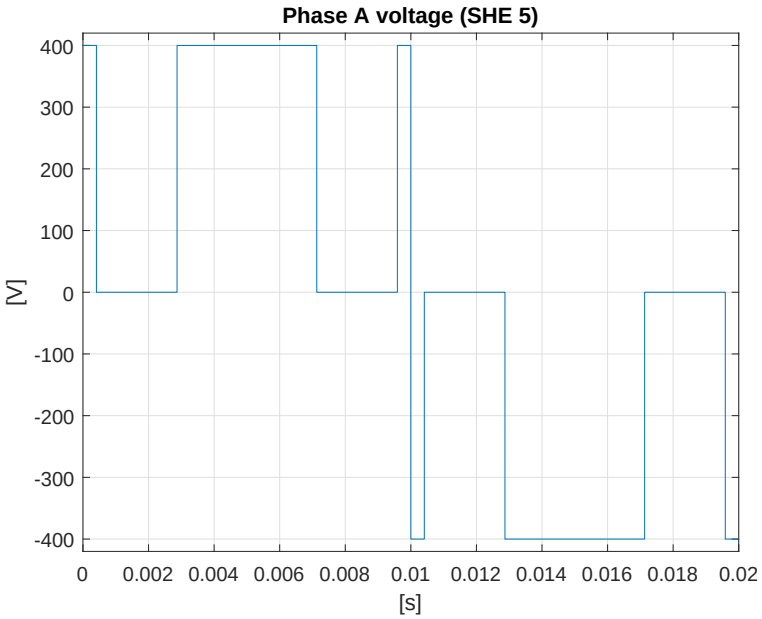

Figure 4.16: Phase A voltage waveform (Selective Harmonic elimination of fifth harmonic)

The waveforms imposed are the voltages produced by the inverter measurable between the central point of a leg and the middle point of the DC link, they contain the homopolar component too.
Obviously the actual phase voltage of the machine won't contain third harmonic and harmonics whose order is multiple of three.
These voltage components constitute the homopolar component. There isn't any phase shift between the "third harmonic" components of each phase, this means that they can not produce any current because that would violate the Kirchhoff's current law as the central point of the star connected stator winding is isolated.
That being said homopolar component voltages will manifest between the central point of the stator winding and the middle point of the DC link of the inverter.

Gazing at the FFT of the current vector (figure 4.17) is possible to notice that the fifth harmonic isn't perfectly zero but it sums up to the very small percentage of the fundamental. The cause of this is probably the time step of the simulation ($50[\mu s]$) that is responsible of a not perfect commutating instant for the voltage wave.

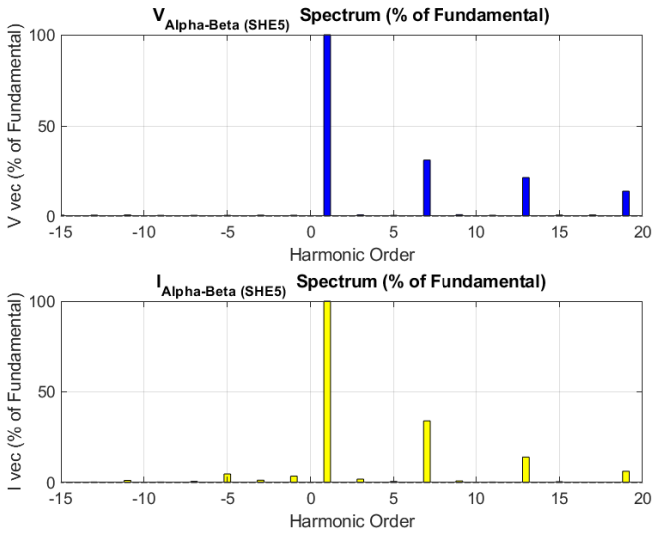

Figure 4.17: Spectrum of voltage and current spatial vectors (Stationary reference frame)

As happened in the previous simulation, the good matching between the FEM computed and the post-processing estimated Torque Harmonic content is confirmed even in this case, it's evident in figure 4.18 where the waveform almost perfectly superimpose.

This happens because of the big magnitude of low frequency harmonics in the current and therefore in the torque. In this configuration they are way more relevant respect to the high frequency ones due to slotting.
Figure 4.19 shows the low frequency harmonics matching.

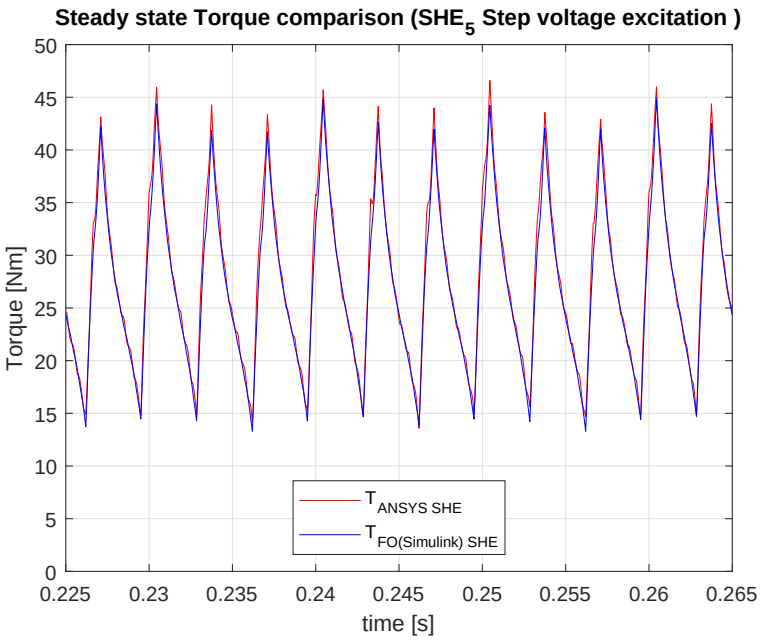

Figure 4.18: SHE excitation steady state Torque (FEM vs Flux observer post-processing)

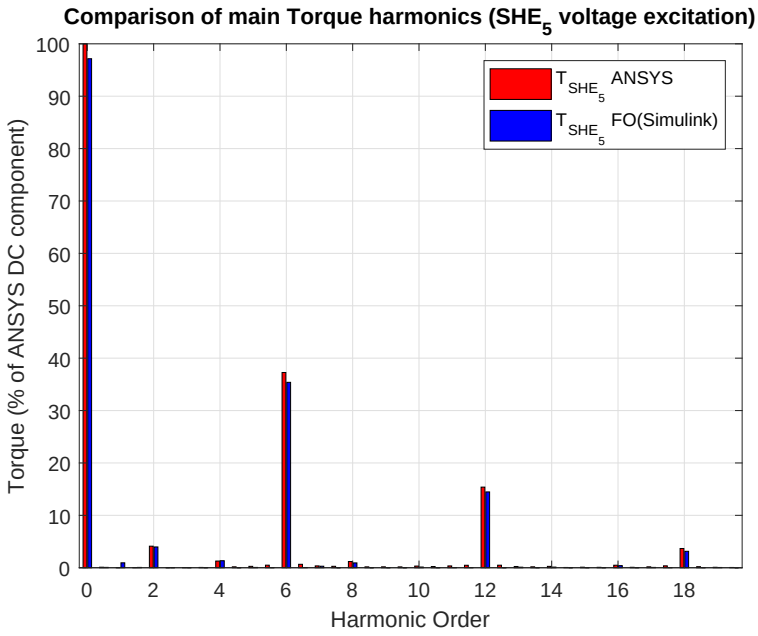

Figure 4.19: Torque Spectrum (FEM vs Flux observer post-processing)

It is worth underlining that eliminating the fifth harmonic of current does not necessarily mean that the sixth harmonic of torque will be reduced respect to the six step case.
Eliminating a harmonic implies a modification of the whole spectrum of the signal, so that guarantees a certain harmonic to be zero, not the *THD* to be lower than the six step case. For example in this case eliminating the fifth harmonic of the current causes the seventh to grow bigger.

4.5 Q-axis current for torque ripple estimation

The main responsible for torque harmonics are the q-axis current harmonics.

By post-processing simulation data is possible to get the spectra of FEM computed torque and q-axis estimated current in the rotor flux aligned frame.
Computing the ratio between these two quantities for the principal harmonics (4.3 where h is the harmonic order) we notice that it's almost constant.

$$R_{\frac{T}{I_q},h} = \frac{T_h}{I_{q,h}} \tag{4.3}$$

Tables 4.1 and 4.2 show the results for the higher amplitude harmonics in the case of six step and selective harmonic elimination aiming at eliminating the fifth harmonic.

This give us an important tool that, for example, can be used for predicting torque harmonics, or torque *THD*.

Harmonic order	$Frequency[Hz]$	$R_{\frac{T}{Iq},h}$	$T_h(estimated)[Nm]$	$Iq_h[A]$
0	0	2.5	27	11
6	300	2.4	6	2.5
12	600	2	0.9	0.5
18	900	1.6	0.3	0.2

Table 4.1: Torque and q-axis current harmonic relationship (Six step voltage excitation)

Harmonic order	$Frequency[Hz]$	$R_{\frac{T}{Iq},h}$	$T_h(estimated)[Nm]$	$Iq_h[A]$
0	0	2.5	27	10.9
6	300	2.5	10	3.8
12	600	2.5	4	1.5
18	900	2.3	1	0.4

Table 4.2: Torque and q-axis current harmonic relationship (SHE voltage excitation)

To give a brief theoretical justification of that we should consider the machine's equations in field oriented frame(4.4, 4.5, 4.6).

$$\frac{d\left|\boldsymbol{\lambda}_r^{\lambda}\right|}{dt} + \frac{R_r}{L_r}\left|\boldsymbol{\lambda}_r^{\lambda}\right| = \frac{R_r}{L_r} L_m \cdot i_{s,d}^{\lambda} \tag{4.4}$$

$$\Lambda_r = \frac{L_m}{1 + s\tau_r} \cdot I_{s,d} \tag{4.5}$$

$$\mathrm{T} = \frac{3}{2} p \frac{L_m}{L_R} \cdot (\lambda_{r,d}^{\lambda} i_{s,q}^{\lambda}) \tag{4.6}$$

Where 4.5 is the Laplace transform of 4.4.
4.5 helps to understand why harmonics of d-axis current cause harmonics with reduced magnitude in the flux, they have to pass through a low pass filter.
Torque equation 4.6 explains why q-axis current harmonics reflect directly in torque harmonics.

A visual feedback of how much precisely q axis current harmonics can predict torque ones is given by the spectra in figures 4.20 and 4.21.
On the right side of the pictures are showed the spectra of the torque computed by the FEM simulation with six step and selective harmonic elimination excitation.
On the left there's the "cleaned" torque spectrum. This is obtained by subtracting from the main harmonics the estimated ones.
In other words, only for each harmonic h listed in tables 4.2 and 4.1, was computed a new torque

harmonic at that frequency:

$$T_{clean,h}(t) = T_{Ansys,h}(t) - T_{estimated,h}(t)$$

The title of each graph shows the *THD* of the torque.
It's worth underlining that the "cleaned" torque waveform present a way lower *THD*. This confirms one time more the accuracy of precision in predicting low frequency torque harmonics using q axis current harmonics.

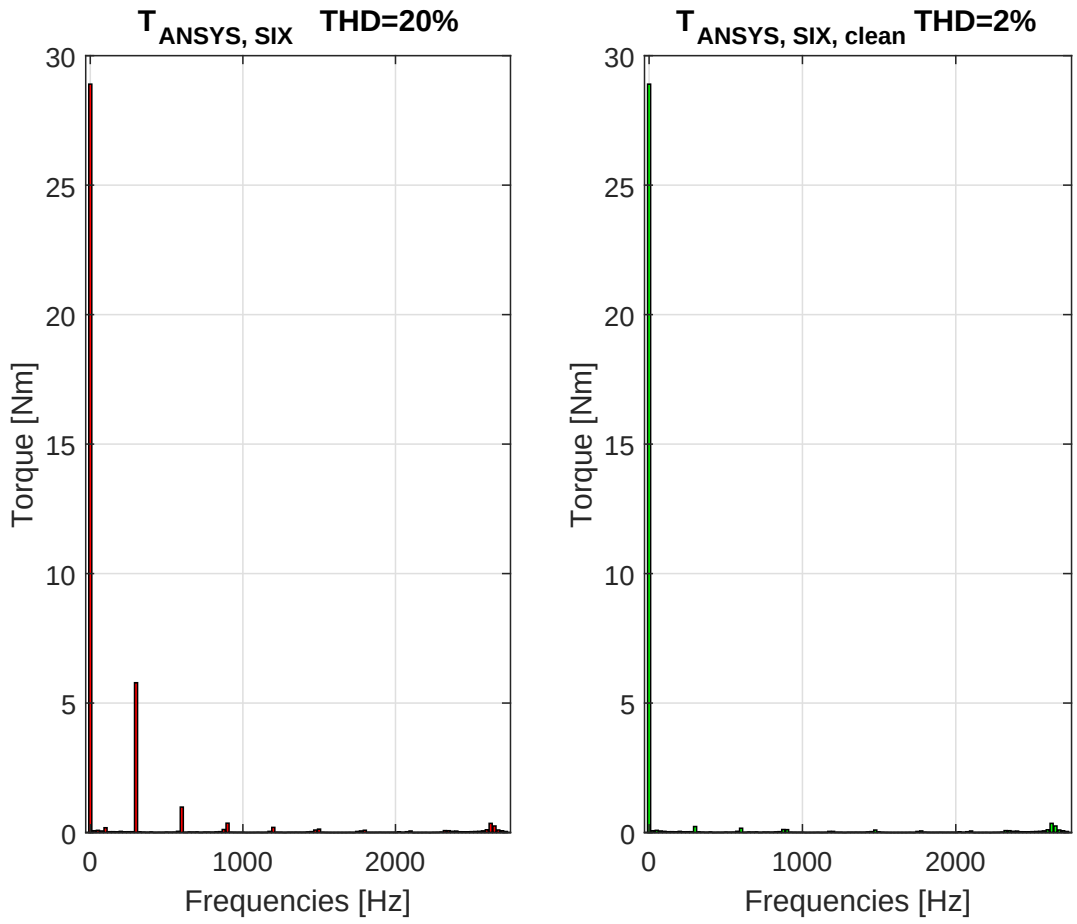

Figure 4.20: Torque spectrum comparison before and after harmonic "cleaning" via q axis current harmonics (Six step voltage)

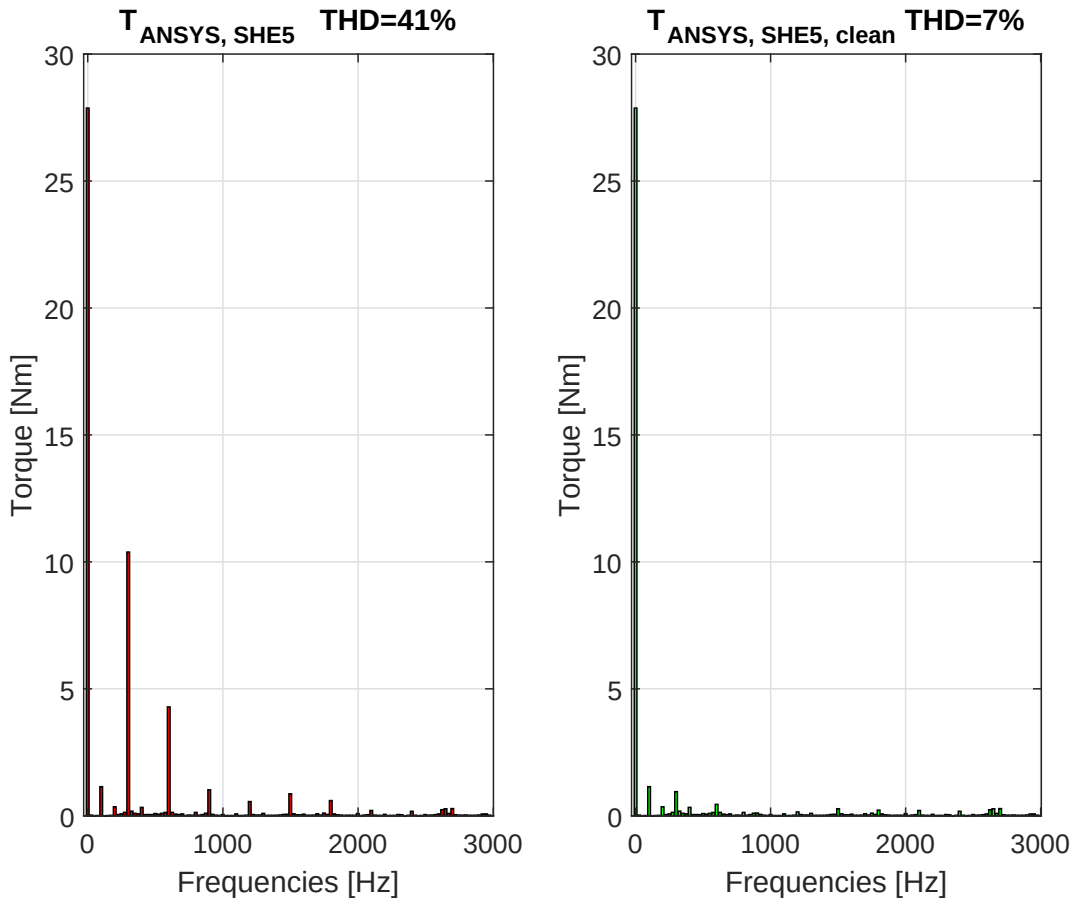

Figure 4.21: Torque spectrum comparison before and after harmonic "cleaning" via q axis current harmonics (SHE voltage)

5

Evaluation of the optimal voltage and slip values for a given torque and speed requirement

There are various combinations of voltage magnitude and fundamental frequency that allow induction motors to operate with given values of torque and rotor speed, keeping into account that there are voltage and current constraints that must be respected.
Therefore it is interesting to investigate the different possibilities in order to choose the best one.
It's worth to underline that the optimum solution could not correspond to the one that minimizes the overall losses as there are other factors that must be considered, and their importance changes with the specific application.
For example, in the railway traction field, could be preferred an operating point that doesn't correspond to the minimum losses one but the majority of losses it presents take place where it's easier to remove the heat. Another issue could be keeping a flux level that would allow a fast enough remagnetization of the machine so a good dynamic response. Furthermore different modulation strategies could be compared.
More likely the best solution will be a trade-off between the aspects listed before and probably many others.

That being said, in this chapter we will describe the test we run with the FEM simulated machine.
The technique used for guessing the right voltage and frequency couple of values that cause the machine to work in the desired operating point is described. We then proceed to compare the losses in their totality and breaking them down in the different components for the various combinations

of $V\&f$ in a fixed mechanical operating point.

Future research in this topic should include the typical non-sinusoidal excitation waveforms employed in railway traction, as well as different design configurations such as the stator rewinding to increase the power density or reduce the size of the machine [4].
Another issue could be the development of trustworthy analytical models of the machine capable of precisely estimate its behaviour in every alimentation condition. This would slim the computational time that is necessarily longer when relying on FEM simulations.

5.1 Voltage tuning

After fixing a precise rotor speed and torque, we wanted to compare, in terms of losses, the different combinations of sinusoidal voltage magnitude and frequency that would cause the machine to work in that point.
Voltage magnitude and frequency as well as rotor speed are the inputs for the FEM simulation, Torque and losses are an output.
We didn't posses a precise a priori knowledge of the output torque that the simulated machine would produce as a consequence of a fixed value of the three input quantities.
To get an estimation of that we relied on the FEM extracted parameters, which were obtained as described in section 3.3.

Firstly we selected a certain range of voltages and frequencies starting from a frequency that causes the synchronous speed to be just a little bit above the fixed rotor speed value.
Then, relying on the classical equivalent circuit we estimated the value of torque produced by each one of the $V\&f$ combinations, producing a plot like the one of figure 5.1.
Starting from that, we plotted the contour for the desired torque value(figure 5.2) and extracted the data corresponding to the contour line of interest.
About ten couples of $V\&f$ values were chosen as input for the FEM simulation.

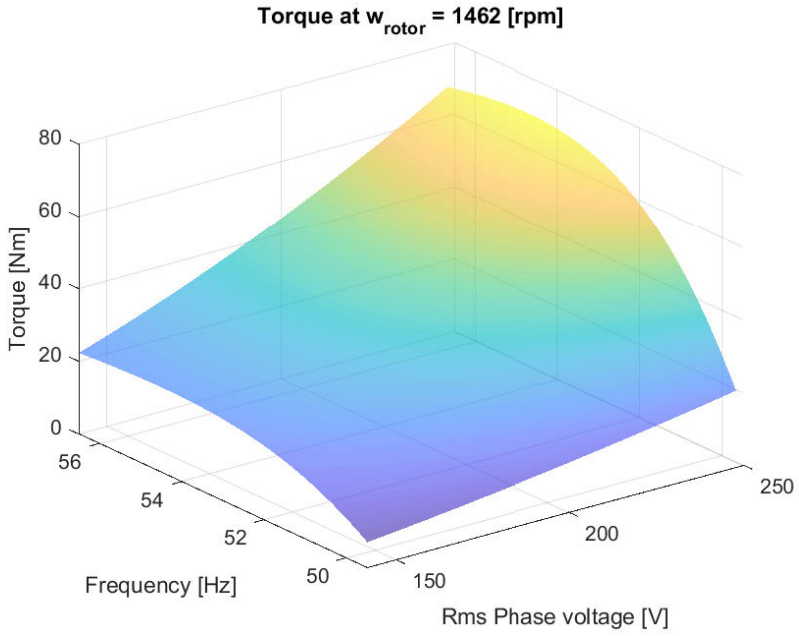

Figure 5.1: Torque values for different combinations of Voltage and frequency (estimated with the analytical model)

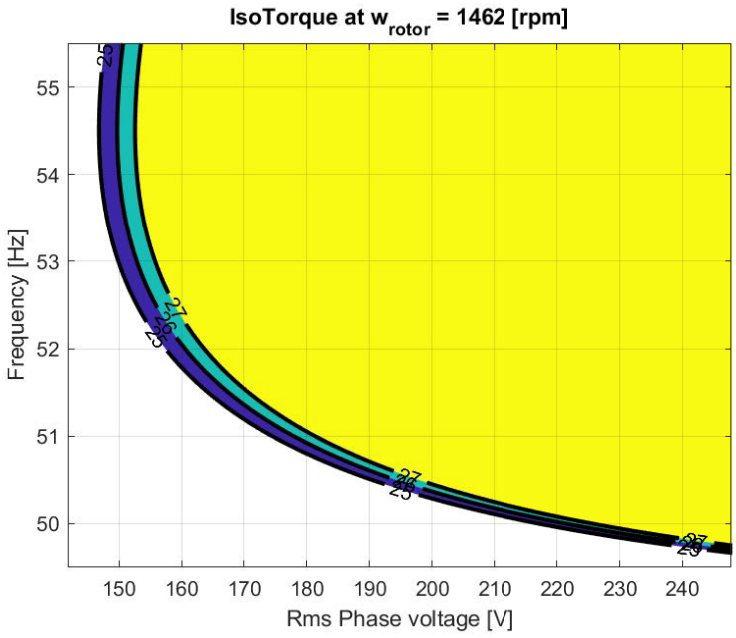

Figure 5.2: Isotorque at desired levels for different combinations of voltage and frequency

We made sure to select couples of values with the frequency increasing until reaching the combination of V & f such that the desired toque corresponded to the breaking torque, the peak value

of the torque versus speed characteristic(figure 5.3).

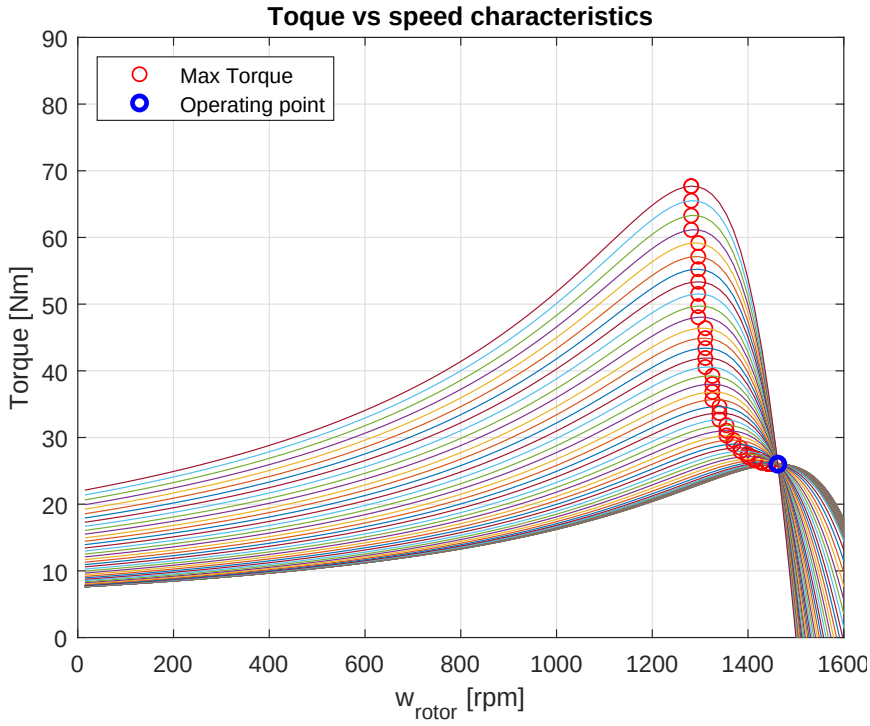

Figure 5.3: Torque versus speed characteristics for "high" frequency (until breaking torque equals the desired torque)

A trial and error procedure was necessary to "tune" the voltage magnitude such that the output torque is the desired one.
For each couple of $V\&f$ values three simulations were run, with fixed frequency and varying the voltage amplitude of $\pm 3[V]$.
Post-processing of the simulation data allowed to compute the right voltage value assuming that for a fixed fundamental frequency and rotor speed the relationship between voltage and torque variations were linear.
Assumption that has revealed to be correct as the output torque corresponded to the desired one in the second simulation run with the perfect voltage value.
Figure 5.4 shows the voltage values of the initial guess and the perfect ones computed in the post-processing.

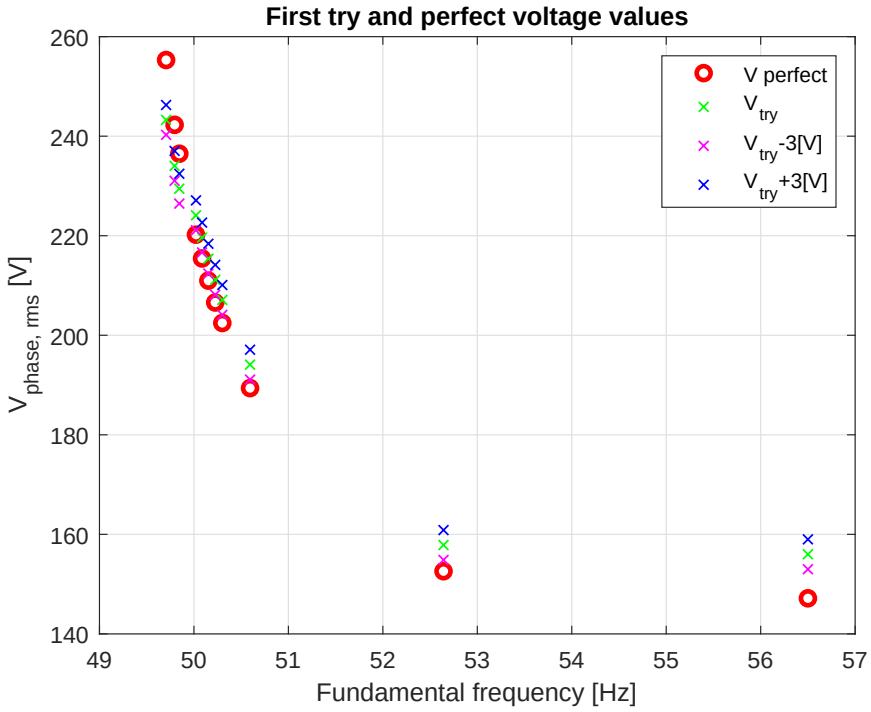

Figure 5.4: First guess and perfect voltage values for "high" frequency simulations

5.2 Losses breakdown

An important aspect of this work was to know not only the losses but breaking them down in the four components:

- Stator and rotor Juole losses
- Stator and rotor Iron losses

The breakdown and total losses, relative to two working points ($\omega_{r,1} = 1462[rpm]$, $T_1 = 27[Nm]$ and $\omega_{r,2} = 147.5[rpm]$, $T_2 = 27[Nm]$) are reported in figures 5.5, 5.6, 5.7 and 5.8.
In figures 5.5 and 5.6 we marked the two points corresponding to the minimum losses and the *maximum torque per ampere* (MTPA) operating condition.
We estimated the frequency value of the minimum losses point by interpolating all the already calculated points in the losses versus frequency graph and getting the x-axis value corresponding to the minimum of the losses curve. To obtain the perfect value of voltage the same procedure described in the previous section was employed.
Simulation run with the estimated values of frequency and voltage indeed led to the minimum losses point amongst the others.

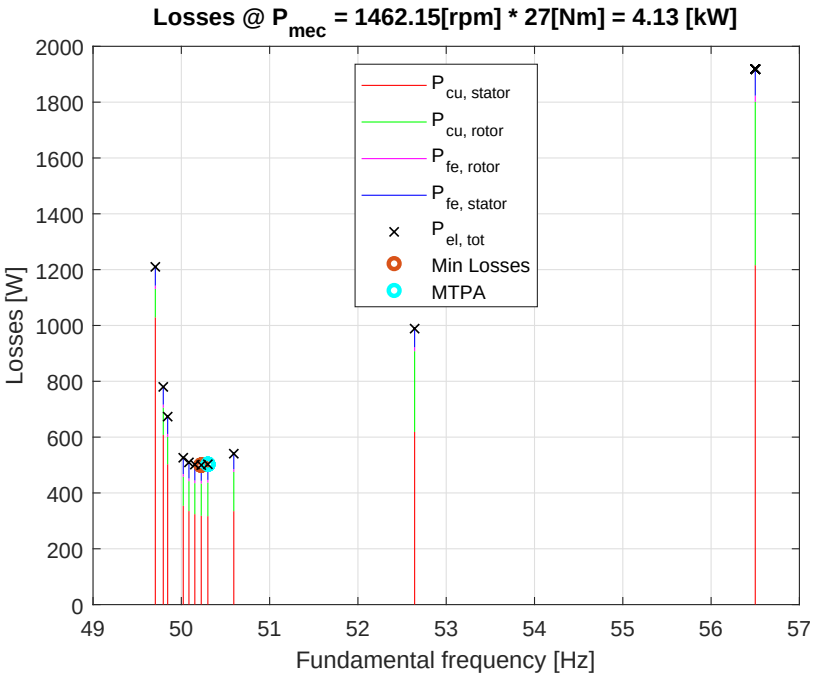

Figure 5.5: Losses for the operating point $\omega_r = 1462[rpm]$ and $T = 27[Nm]$

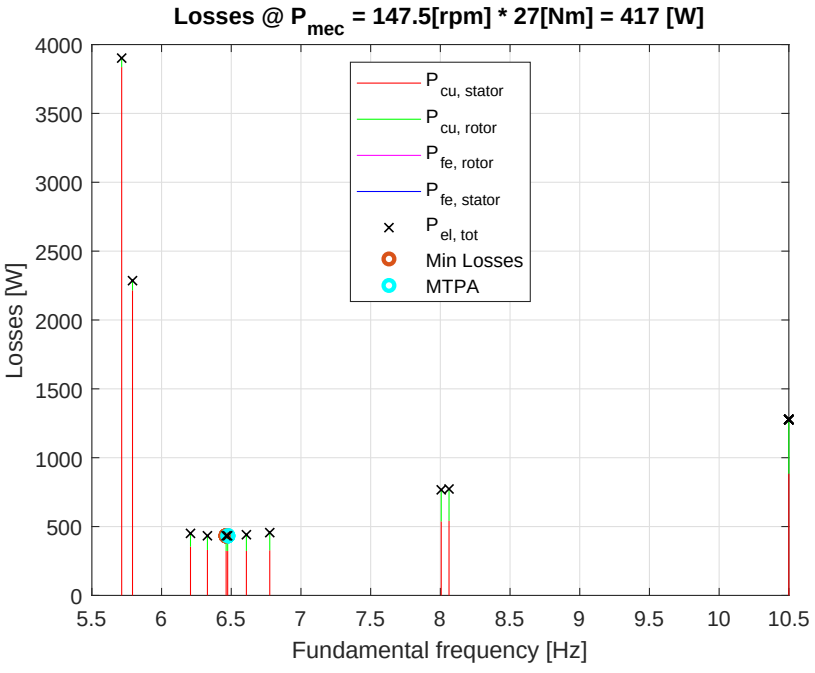

Figure 5.6: Losses for the operating point $\omega_r = 147.5[rpm]$ and $T = 27[Nm]$

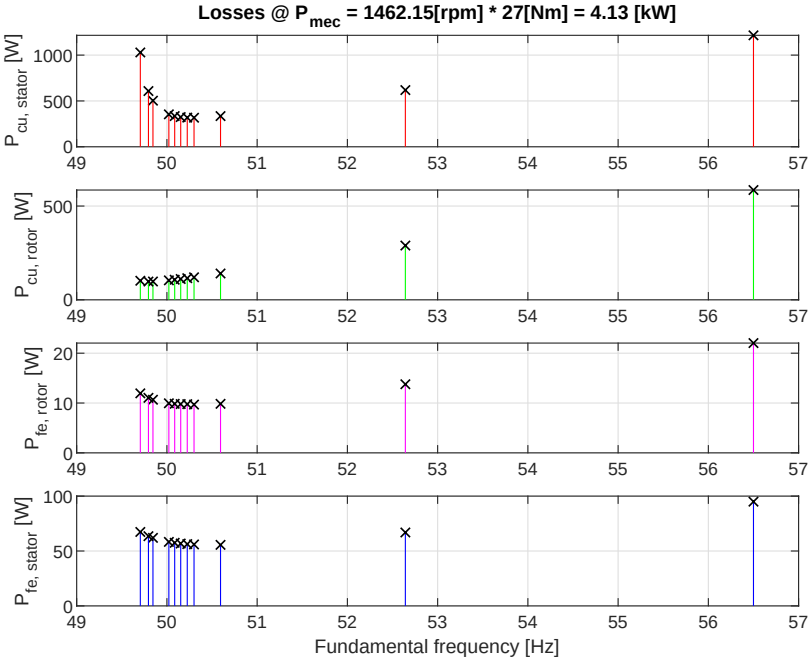

Figure 5.7: Losses breakdown for the operating point $\omega_r = 1462[rpm]$ and $T = 27[Nm]$

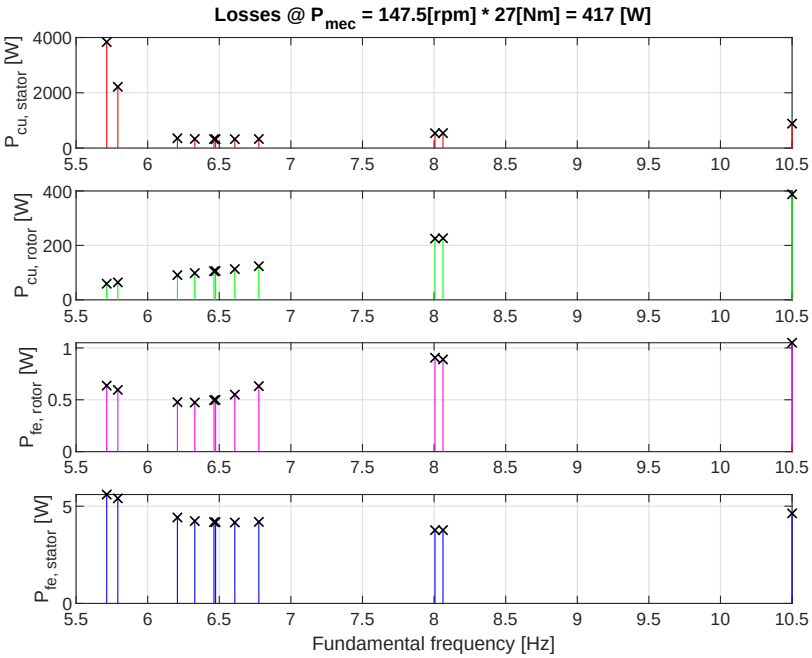

Figure 5.8: Losses breakdown for the operating point $\omega_r = 147.5[rpm]$ and $T = 27[Nm]$

Figures 5.5 and 5.6 put into evidence that the MTPA point doesn't coincide with the minimum

losses one, but the difference, in terms of losses, amongst those two points seems to be negligible, at least for the investigated cases.
As expected from the theory, rotor copper losses grow as the fundamental frequency, or in other words the slip, increases.
Slip values that cause the losses to be minimum always appeared to be between 2% and 3%.

6
Experimental tests

In this chapter we will describe the experimental tests run on the real machine.
It was possible to test only the original one and only with the sinusoidal voltage supply of the three phase distribution grid.
To test experimentally the machines whose stator has been rewinded, or even to test the original one with a non sinusoidal voltage waveform it is necessary to use an inverter. This would allow to produce ”sinusoidal” or non-sinusoidal voltage waveforms and to control their amplitude too, as the rated voltage is lower for the rewinded motors.
The three phase inverter and its proper control are now under construction and will surely be an essential tool to carry out further investigation on this subject.

At first are detailed the test bench configuration, its mounting procedure and the measurement instrumentation employed.
Later on we proceed to analyse torque spectra, computed starting from the output waveform of the torque sensor, relative to the operation of only the load motor, only the test one and both of them.
Then, we go on describing the problem experienced with the drive that made impossible to work with the test motor operating as an actual motor and the load one regenerating.
Finally are reported the performance measurements with the test motor generating at various different rotor speeds (slip values).

To measure the motors input and output powers in various operating conditions we run some experimental tests.

The original motor, the one whose stator winding hasn't been modified, was mounted into a test bench. Its block scheme representation can be found in figure 6.1.

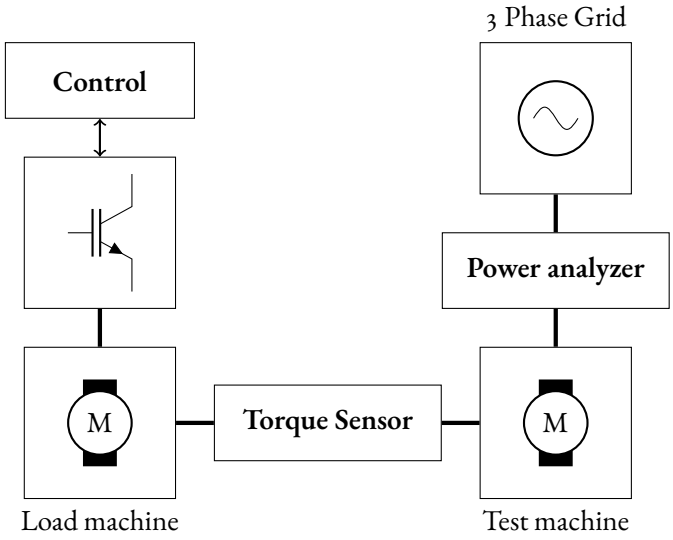

Figure 6.1: Test bench configuration

The measuring of the desired quantities was carried out employing a power analyser, able to measure electrical and mechanical power.
The test bench was already equipped with a $11[kW]$ induction machine whose speed can be controlled by means of a drive(figure 6.2). The connection between the drive and a pc eases the variation of the speed reference. The speed signal produced by the motor's encoder can be used as an input for the power analyser as well.

Before getting to the final configuration (figure 6.1) it was necessary to design, realize and mount various mechanical supports and components.
They were essential to:

- Get the motors axes to the same height;
- Reduce the axis diameter of the bigger motor to make it equal to the one of the smaller in order to use the torque sensor couplings;
- Support the Torque sensor and allow its translation and height regulation;
- Make sure that the angular and linear misalignment among axes and were lower than what the torque sensor allows.

Some of those can be appreciated in figure 6.3.

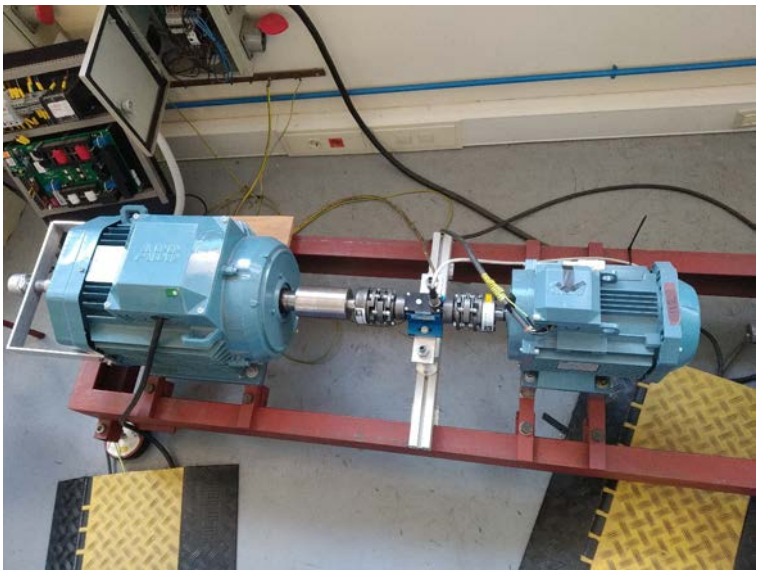

Figure 6.2: Test bench

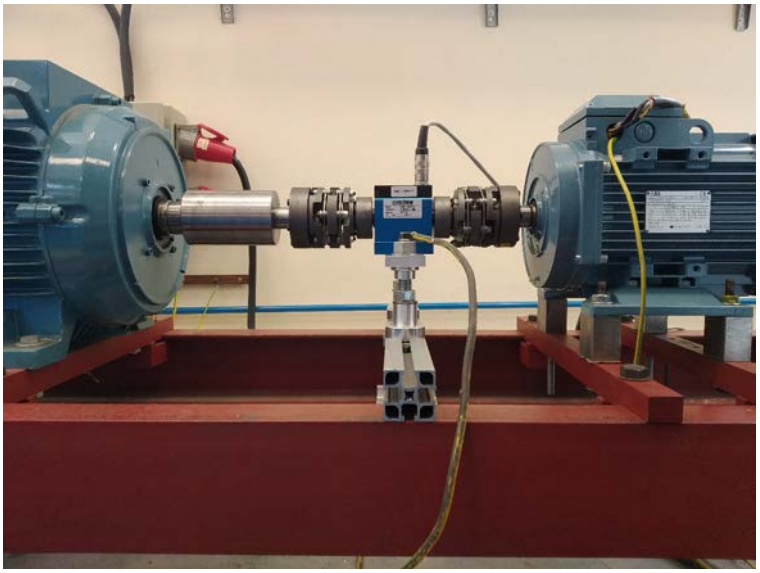

Figure 6.3: Torque sensor and mechanical couplings detail

A DC power supply is used to feed the torque sensor, its output, as well as the one of the encoder, acts as an input for the power analyser. In order to translate the speed signal to the voltage level accepted by the power analyser a voltage divisor had to be implemented, this can be noticed in the board's picture, figure 6.4.

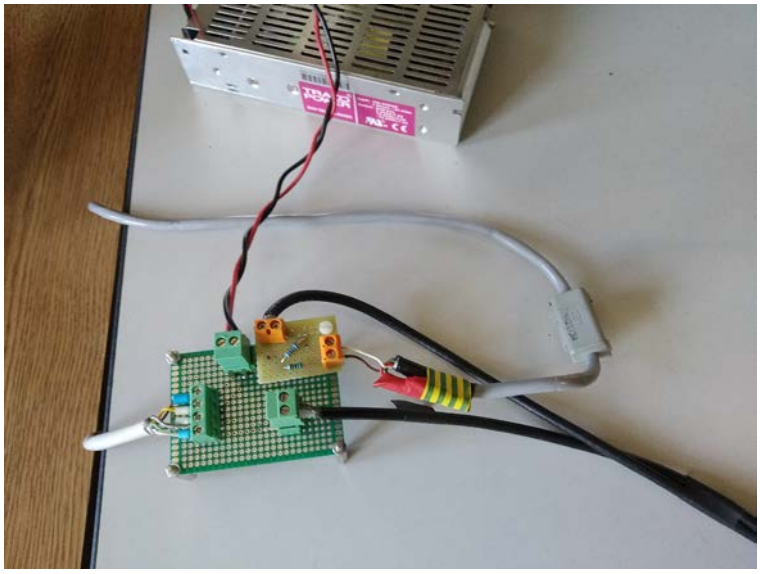

Figure 6.4: Circuit board (feeds the torque sensor and receives the signals of Torque and speed)

We run some trial tests acquiring the detailed torque waveform by means of an oscilloscope. We then post-processed it analysing its FFT, and it was possible to make some considerations:

- In the no load scenario, operating only with the test motor grid connected and the load one disconnected, torque waveform presents an harmonic at $100[Hz]$;
- Operating with both motors, the test one grid connected and the load one imposing the synchronous speed ($1500[rpm]$), we notice a group of harmonics located around $120[Hz]$(figure 6.5), the harmonic at $100[Hz]$ keeps on appearing as the test motor is connected to the grid;
- The presence of this group of harmonics always holds when the inverter fed load motor is operating. This is confirmed by some other tests run at different speeds, in which the test motor, not connected to the grid, acts an a rotating inertia(figure 6.6).

The $100[Hz]$ torque harmonic could be caused by the small unbalance in the three phase voltage of the distribution grid.
If an inverse sequence triad is present in the voltage feeding the motor than it will cause a current responsible for an air gap field rotating at an angular speed which has the same module of the direct triad one but opposite direction. The interaction of this field with the fundamental rotor one produces an alternating torque, with zero mean value, at a frequency equal to the double of the fundamental one [20].
Up to now we didn't manage to justify the presence of the harmonics around $120[Hz]$, that will be a topic for future investigation.

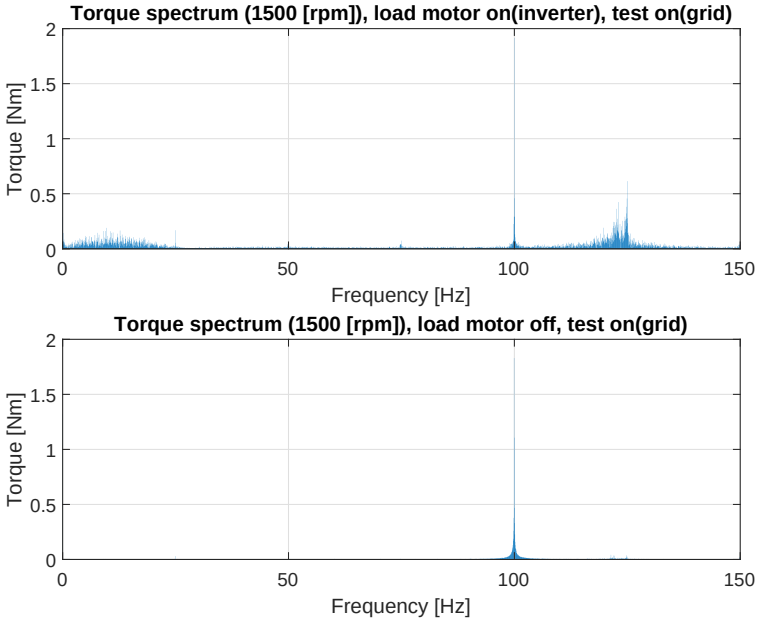

Figure 6.5: Torque spectrum, motors alternatively operating at $1500[rpm]$

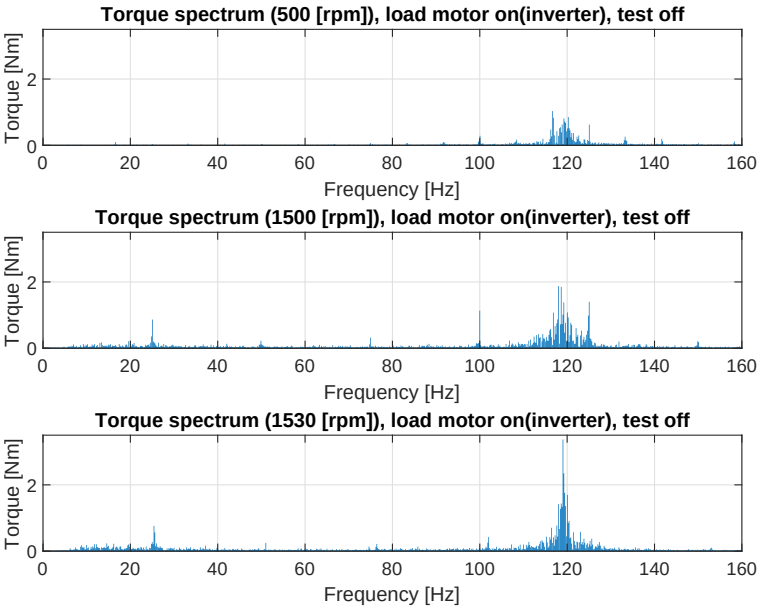

Figure 6.6: Torque spectrum, load motor operating at $500[rpm]$, $1500[rpm]$ and $1530[rpm]$

The objective of these tests is to measure the performance of the motor in various operating points. The test motor is connected to grid, this means that it will always be fed by a three phase sinusoidal voltage at $50[Hz]$ and $400[V]$ RMS line to line.
As a consequence the synchronous speed is fixed too, at $1500[rpm]$ since the motor presents two pole pairs, and to change the operating point we act varying the slip.
To do so we fix the reference rotor speed of the vectorial control of the load motor and, since the two axes are connected, this speed will be the speed of the test motor's rotor as well.

The wiring scheme adopted to measure the electrical power is the $3P4W$ represented in figure 6.7. Figure 6.8 shows the actual wiring in the power analyser, on the right side of the picture the mechanical quantities input cables can be observed.

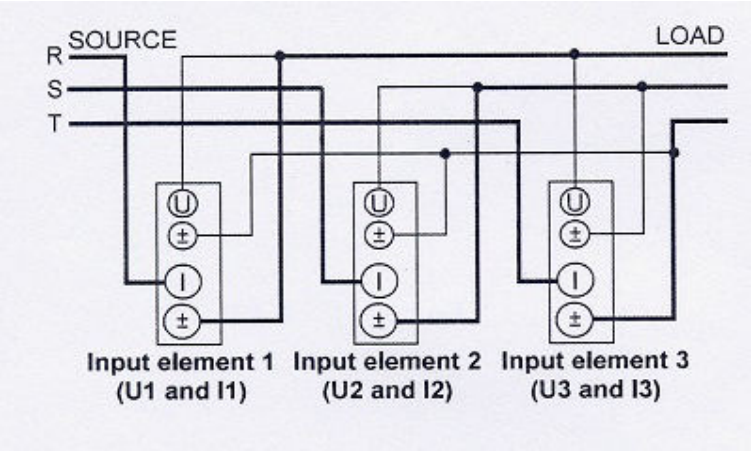

Figure 6.7: 3P4W measurement scheme

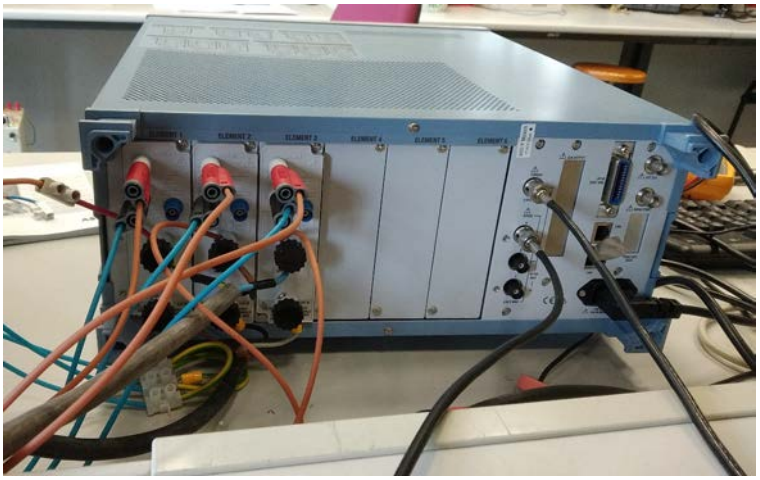

Figure 6.8: Power analyser wiring configuration ($3P4W$)

After verifying the direction of rotation of the motors, the load one was commanded to rotate at $1500[rpm]$ and the test one connected to grid.
The following step was to start reducing the speed imposed to the rotor in order to increase the slip and observe the on load behaviour of the test motor.

By doing so we noticed a problem in the drive of the load motor.
When the test motor operates as an actual motor the load one acts as a generator.
The electric power produced by the load motor flows through the inverter and ends up charging the DC link capacitor. This capacitor keeps on charging, and therefore the voltage at its terminals keeps on rising, until it reaches a certain voltage limit ($700[V]$ in this case). When the voltage limit is reached a transistor receives the command to switch so that the discharge resistance is inserted in parallel to the capacitor.
When this happens a protection makes the drive stop operating because of an overcurrent in the braking transistor.

To avoid this fault we decided to run the test in the negative slip region, making the test motor operating as a generator, with its rotor spinning at speed higher than the synchronous one.

In this section some data acquired with the power analyser are reported. Table 6.1 lists the powers in the various operating points tested, torque and powers are negative because were measured using the motor convention.
As it was expected operating with constant voltage amplitude and varying the slip, the efficiency rises as we get closer to the nominal operating conditions([21]).

$\omega_{rotor}[rpm]$	Torque $[Nm]$	$P_{mec}[W]$	$P_{el}[W]$	η
1504	-4	-620	-375	61%
1509	-7	-1032	-634	61%
1519	-14	-2180	-1500	69%
1530	-21	-3229	-2917	87%
1539	-28	-4457	-3951	89%
1545	-31	-5043	-4320	86%
1551	-37	-5663	-5166	91%
1554	-38	-6331	-5325	84%

Table 6.1: Performance comparison for different slips operating as a generator

Elaborations of the voltage and current measurements allowed to produce the figures 6.9 and 6.10. It is evident the distortion of the current waveform from the ideal sinusoidal shape.
In the sinusoidal case the space vector trajectory is a perfect circle in the $\alpha\beta$ plane, while, if considering a rotating reference frame, synchronous with the electrical pulsation, this trajectory reduces to a point.
What we just affirmed is verifiable in the voltage vector trajectory, which forms an almost perfect circle for every load condition, because the grid impose a sinusoidal three phase voltage at the motor's terminals with just some small unbalances.
By looking at the current vector trajectory we notice something different, the shape is not perfectly circular in the $\alpha\beta$ plane, this is consequence of the not perfectly circular shape of the voltage trajectory, this is probably due to a little imbalance in the three phase voltage of the distribution grid [22].
In the synchronous reference the current trajectory doesn't collapse into a point but harmonic current spatial vectors which have higher frequency than the fundamental one (and present a lower magnitude) end up drawing the green shape we observe in the pictures as they revolve around the tip of the fundamental current vector, which is static in this reference frame.
This is happening because of current harmonics that manifest even in the perfectly sinusoidal voltage alimentation condition.
Those harmonics are due to the presence of air gap flux density harmonic waves that induce *electromotive forces* (EMFs) and therefore currents in the stator winding. Magnetic flux waves can be considered as the product of *magneto motive force* (MMF) wave and permeance wave, both of them present harmonic components.
MMF stator and rotor waves are produced by distributed windings and therefore, at each instant in time, those waves are stepwise, not sinusoidal, and they present a certain spatial harmonic content.
Permeance wave presents harmonics due to the stator and rotor slotting, as well as to saturation

([23], [24]).

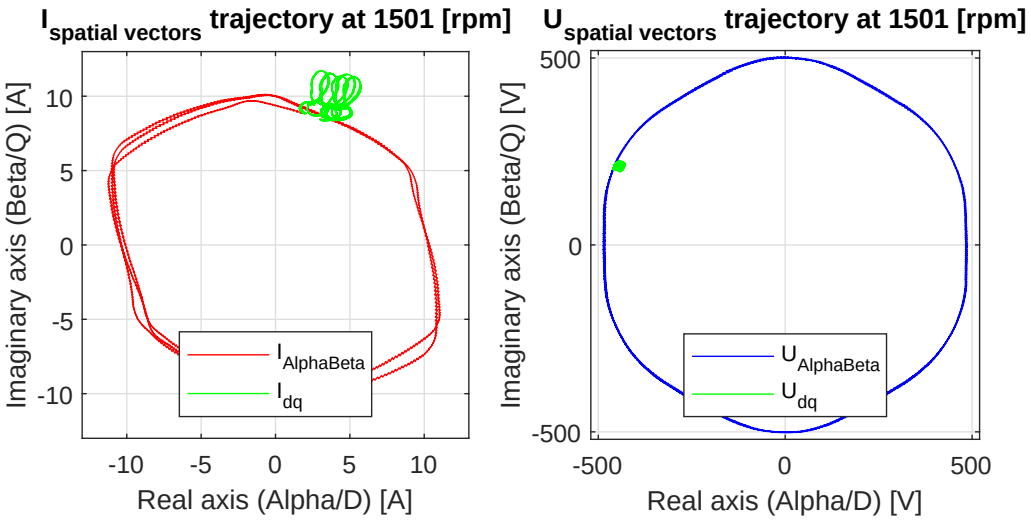

Figure 6.9: Current and voltage spatial vectors trajectory in static and synchronous reference frame ($\omega_{rotor} = 1501[rpm]$)

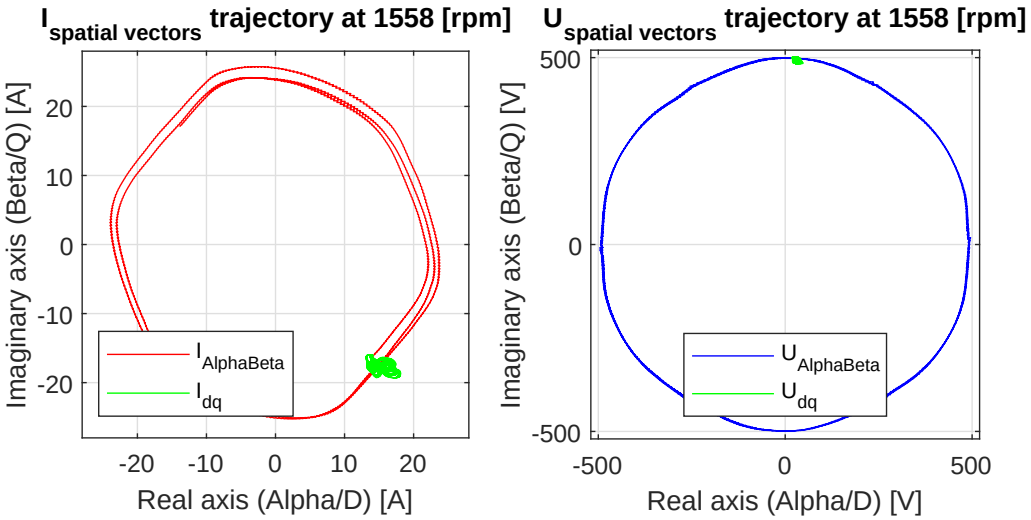

Figure 6.10: Current and voltage spatial vectors trajectory in static and synchronous reference frame ($\omega_{rotor} = 1558[rpm]$)

In figures 6.12 and 6.11 it is noticeable that the power generated by the machine is not equally divided in each phase. This unbalance does not completely disappear as the load increases but when we increase the magnitude of the slip, as we can see in the graphs, it tends to reduce.
When summing the power absorbed by each phase in a perfectly balanced three phase load, fed by a symmetrical set of three phase voltages, is well know that the result is a constant value, as reported in figure 6.13.

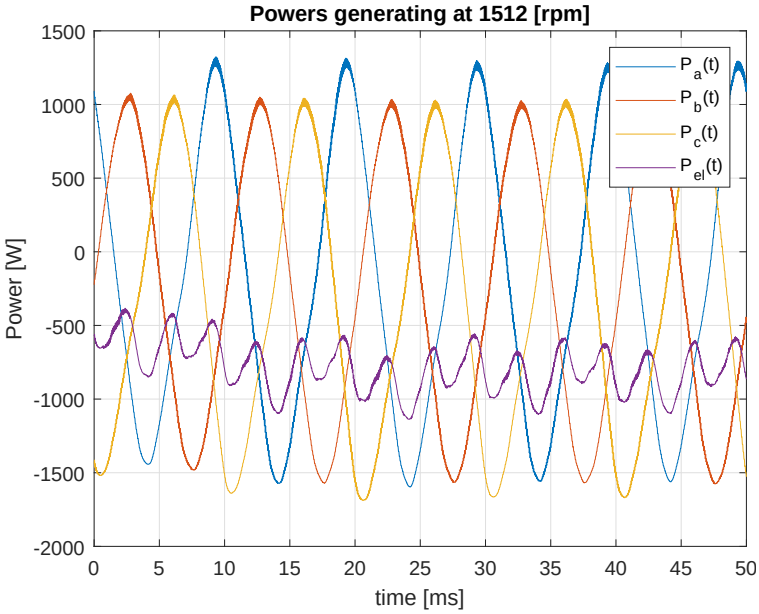

Figure 6.11: Single phase and three phase instantaneous powers ($\omega_{rotor} = 1512[rpm]$)

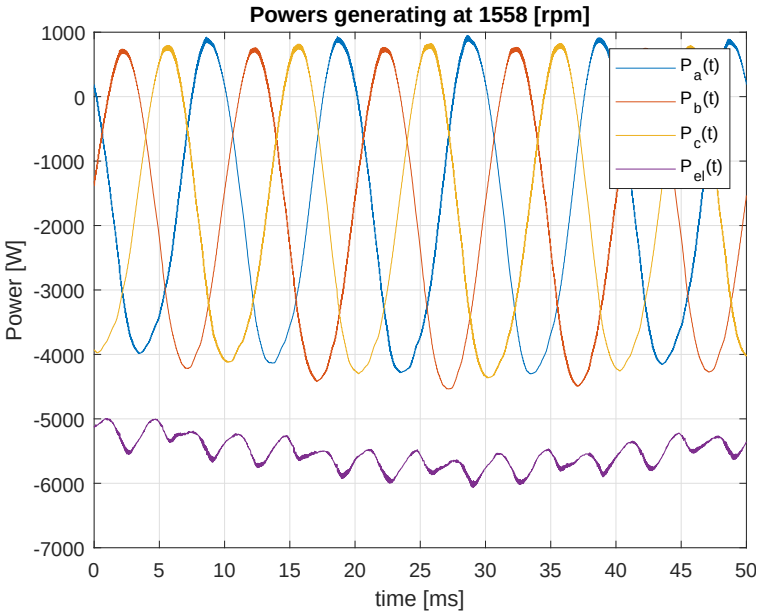

Figure 6.12: Single phase and three phase instantaneous powers ($\omega_{rotor} = 1558[rpm]$)

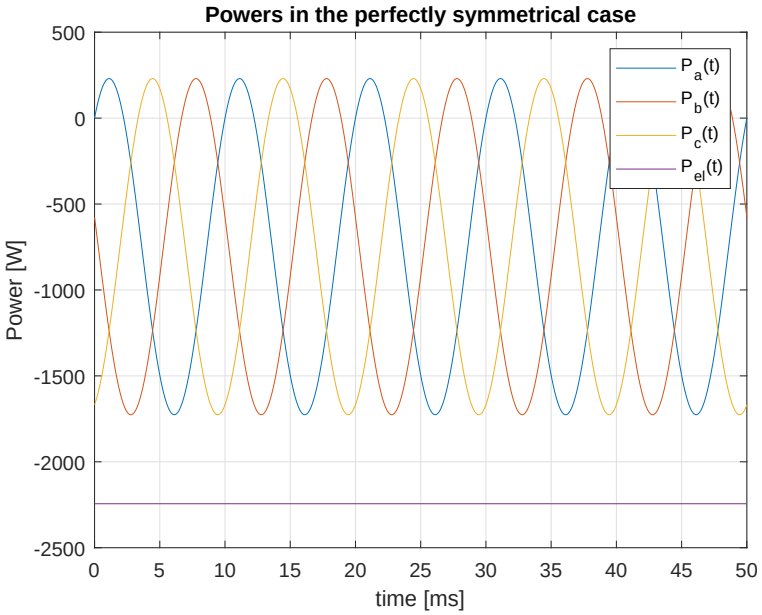

Figure 6.13: Power in the perfect three phase symmetrical case

The unbalanced distribution of power among phases that emerged from the experimental tests we run showed in terms of active power that for each slip condition: $P_{U1} < P_{V1} < P_{W1}$.
In order to justify what happened, and understand if the problem was caused by an unbalance in the grid voltage or in the stator winding another test was run.
This time we made the load motor impose $\omega_{rotor} = 1535[rpm]$ and performed three measurements operating a permutation of the connection between the phases of the grid and the ones of the motor.

$\omega_{rotor}[rpm]$	$P_{el}[W]$	$P_{U1}[W]$	$P_{V1}[W]$	$P_{W1}[W]$
1536	-3520	-1091	-1184	-1245
1536	-3840	-1214	-1349	-1277
1534	-3518	-1023	-1254	-1241

Table 6.2: Active power produced by each phase in the same slip condition (permutation of grid connection)

Results reported in table 6.2 put into evidence that the phase $U1$ is always interested by a lower amount of active power respect to the others.
This suggests that an unbalance is present on the phase $U1$ winding of the motor.

In figures 6.14 and 6.15 we compared the performance, in terms of torque and active power,

of the real machine and the one simulated with FEM. For the simulation we fixed the same rotor speed and voltage with the same peak value of the one measured for the phase a of the machine, so neglected the grid voltage unbalance.
It is evident that the results don't exhibit a good match.
The responsibility for this can be imputed to combined effect of the dissymmetry of the stator windings, the lack of knowledge about the material characteristics of the real motor and the grid's voltage unbalance. Other minor issues affecting this, with smaller impact, can surely be the presence of the cooling fan in the real motor that it's not taken into account in the FEM model and the uncertainty of the measuring instruments employed for the test bench measurements.

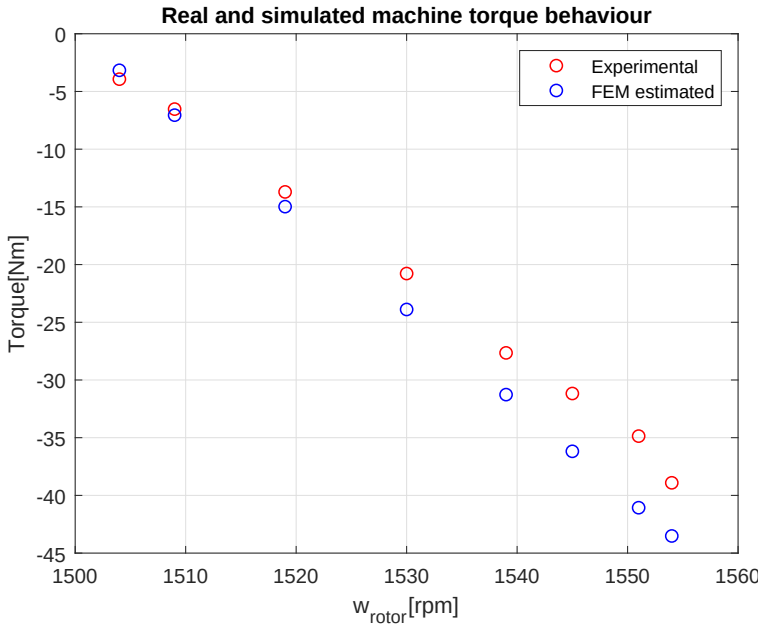

Figure 6.14: Comparison of real and simulated machine torque for various slip values (generating)

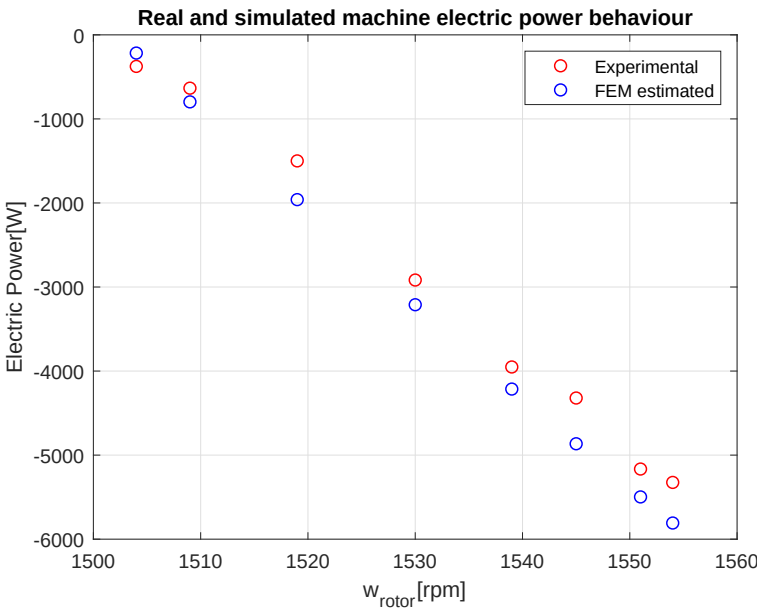

Figure 6.15: Comparison of real and simulated machine active powers for various slip values (generating)

7 Conclusion

In this work we implemented and then tested different tools for predicting the performance of induction machines.
Starting by building a FEM model of the machine we immediately noticed how sensible its output was to different geometry and materials.
We relied on this model to extract the parameters later used in the two analytical models we implemented. Those managed to predict machine's performance for the sinusoidal rated load case with an accuracy that didn't worsened when the harmonic content of the voltage excitation waveform increased.
Anyway those models revealed to be still far from being able to give a trustworthy estimation that could replicate *finite element analysis* (FEA) results with high accuracy.
A flux observer has been employed for post-processing the FEA data. It managed to accurately predict the torque pulsations due to q axis current harmonics.
FEA has been useful as well for comparing the different possibilities of alimentation that can cause the motor to work in the same mechanical operating point and make some considerations about the more convenient. This allowed to underline how, for example, the MTPA operation doesn't necessary coincide with the minimum losses one even though the differences, in the investigated cases, have revealed to be small.
Experimental setup involving a test bench, a load motor controlled by a drive, the test motor and measuring utilities has been mounted allowing the comparison of the FEA and real machine behaviour (while working as a generator).
Concerning this, discrepancies among FEA results and experimental tests have exhibited. Once more we realized how difficult it is to build a reliable model without knowing the characteristics of

the machine's materials. Another part of the responsibility of that has to be given to the unbalance of motor's phases.

7.1 Future work

Here we wish to present the future work that should be carried out about issues that we weren't able to properly conclude in this thesis, but as well some suggestions regarding issues that weren't a target of this work but in the author's opinion, in the light of what he learned in the process of developing this thesis, deserve further analysis.

Torque pulsations prediction via q axis current harmonics has revealed to work well. Future research starting from this fact could, for example, aim at developing control strategies and switching patterns with the objective of orienting current harmonics in the d axis. In this case they will be filtered by the dynamics of the magnetizing inductance and wouldn't reflect so strongly in torque harmonics.

Concerning the comparison of different alimentation possibilities would be interesting to take into account various non-sinusoidal excitation strategies and the dynamic requirements of the specific application [25]. Furthermore, the development of trustworthy analytical models for various alimentation conditions would slim the computational time required for the analysis.

The fact that we couldn't, up to now, dispose of a controlled inverter to feed the test motors didn't allow us to perform experimental tests with the rewinded machines and using non-sinusoidal voltage waveforms.
This will be for sure a matter of future investigation, as well as the refinement of the FEM model. The thermal aspect of the problem wasn't taken into consideration up to now but including it, in future research, would be important for the exhaustiveness of the study.

A

High frequency equivalent circuit of induction motor

The classic per-phase steady state equivalent circuit for Induction motors, that neglects the iron losses, is presented in figure A.1.

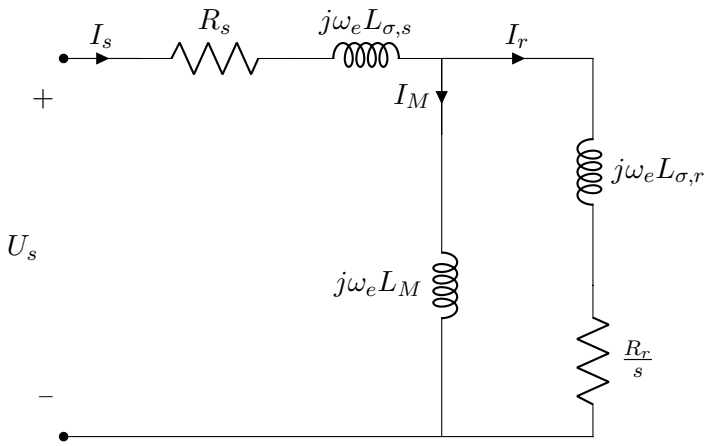

Figure A.1: Per-Phase steady state equivalent circuit of Induction motor (no core losses)

By means of algebraic manipulations is possible to transform that in another steady state equivalent circuit (figure A.2).
We introduced the parameter a but is important to underline that the equivalent impedance of the

circuit is the same as the one of figure A.1 and results independent from a.
It's possible to demonstrate that both of those equivalent impedances are:

$$\underline{Z_{eq}} = \frac{R_s \frac{R_r}{s} + \omega_e^2 \left(L_M^2 - L_s L_M\right) + j\omega_e \left(\frac{R_r}{s} L_s + L_r R_s\right)}{\frac{R_r}{s} + j\omega_e L_r}$$

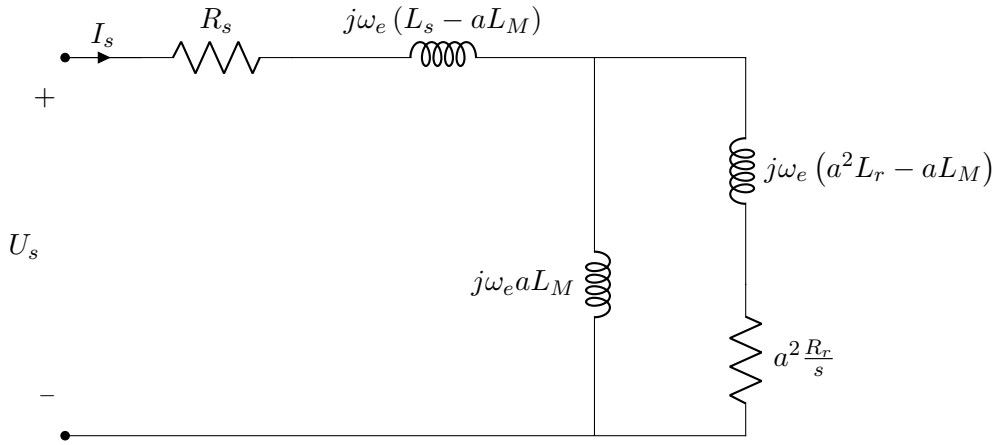

Figure A.2: Modified steady state equivalent circuit of Induction motor (same equivalent impedance of the classic one)

Something interesting happens if we substitute $a = \frac{L_M}{L_r}$.
As we can see in figure A.3, the leakage inductance appears only on the "stator side" and the two parallel branches are constituted by a pure resistance and a pure inductive reactance.
This means that they will be interested by two currents in quadrature one respect to the other.

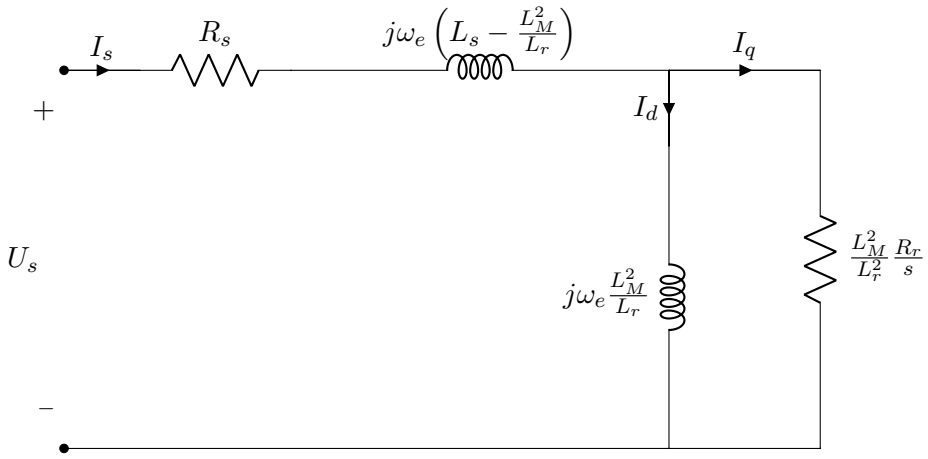

Figure A.3: Steady state equivalent circuit of Induction motor (with all leakage inductances on "stator side")

Employing spatial vectors notation and FOC models helps to simplify the equations involved in the description of machine's behaviour and the understanding of control strategies.
Spatial vectors are obtained by means of an algebraic transformation of the phase quantities. By doing so we are able, employing a single vector, to describe the behaviour of the whole three-phase system. Transformation of phase quantities to a static reference frame (*Alpha-Beta*) is done by means of the equation A.1 .
The multiplying factor $\frac{2}{3}$ guarantees the conservation of the amplitudes, in other words, for a balanced three phase system: $|\boldsymbol{I}_{\alpha\beta}| = \hat{I}_a (= \hat{I}_b = \hat{I}_c)$.

$$\boldsymbol{I}_{\alpha\beta} = \frac{2}{3} \cdot \left(i_a + i_b e^{j\frac{2}{3}\pi} + i_c e^{j\frac{4}{3}\pi} \right) \tag{A.1}$$

Using a reference frame which rotates at an angular speed equal to the electrical pulsation and whose direct axis is aligned with the rotor flux spatial vector ($|\boldsymbol{\lambda_r}| = \lambda_{r,d}$ and $\lambda_{r,q} = 0$) leads to a further simplification of the dynamic (for example A.2, A.3) and torque (A.4) equations of the machine.

$$\boldsymbol{v}_{dq,s}^{\lambda_r} = R_s \boldsymbol{i}_{dq,s}^{\lambda_r} + \underbrace{\frac{d\boldsymbol{\lambda}_{dq,s}^{\lambda_r}}{dt}}_{=0 \text{ in steady state}} + j\omega_e \boldsymbol{\lambda}_{dq,s}^{\lambda_r} \tag{A.2}$$

$$\boldsymbol{\lambda}_{dq,s}^{\lambda_r} = \frac{L_m}{L_r} \boldsymbol{\lambda}_{dq,r}^{\lambda_r} + \left(L_s - \frac{L_M^2}{L_r} \right) \boldsymbol{i}_{dq,s}^{\lambda_r} \tag{A.3}$$

$$T = \frac{3}{2}\frac{L_m}{L_r} p\left(\lambda_{R,d} \cdot i_{S,q}\right) \tag{A.4}$$

In order to use A.4 to compute torque, the spatial vectors of current and flux must have a magnitude equal to the peak value of these quantities, if we use the *root mean square* (RMS) values, the multiplying factor $\frac{3}{2}$ must be substituted with 3.

Figure A.3 gives the circuit representation of equations A.2 and A.3 and it evidences the d and q axis components of the stator current which respectively represent the flux and the torque producing components.

Given that reactances increase proportionally to frequency, when dealing with high frequencies, it's legit to neglect the parallel branch that hosts the magnetizing reactance. By doing so, starting from circuit A.3, we obtain the equivalent circuit represented in figure A.4.

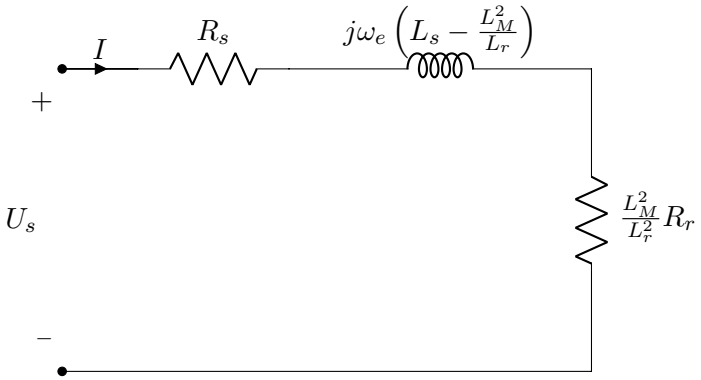

Figure A.4: Per-Phase high frequency equivalent circuit of Induction motor

References

[1] M. N. Uddin and S. W. Nam, "New online loss-minimization-based control of an induction motor drive," *IEEE transactions on Power Electronics*, vol. 23, no. 2, pp. 926–933, 2008.

[2] A. M. Bazzi and P. T. Krein, "Review of methods for real-time loss minimization in induction machines," *IEEE Transactions on Industry Applications*, vol. 46, no. 6, pp. 2319–2328, 2010.

[3] L. Buhrkall, "Traction system case study," in *2008 IET Professional Development course on Electric Traction Systems*. IET, 2008, pp. 45–63.

[4] R. Ikeda, S. Yusya, and K. Kondo, "Study on design method for increasing power density of induction motors for electric railway vehicle traction," in *2019 IEEE International Electric Machines & Drives Conference (IEMDC)*. IEEE, 2019, pp. 1545–1550.

[5] Y. Liu and A. M. Bazzi, "A general analytical three-phase induction machine core loss model in the arbitrary reference frame," *IEEE Transactions on Industry Applications*, vol. 53, no. 5, pp. 4210–4220, 2017.

[6] N. Bianchi, *Calcolo delle macchine elettriche col metodo degli elementi finiti*. Cleup, 2001.

[7] N. Bianchi and S. Bolognani, *Metodologie di progettazione delle macchine elettriche*. Cleup, 2001.

[8] M. Andriollo, G. Martinelli, A. Morini, and A. Tortella, *Macchine Elettriche Rotanti. Teoria ed Esercizi*. Società Editrice Esculapio, 2019.

[9] S. Jurkovic, "Induction motor parameters extraction," *Educypedia-Electronics*, 2014.

[10] F. Briz, "Lecture notes of dynamic control of ac machines," 2019.

[11] W. A. Roshen, "A practical, accurate and very general core loss model for nonsinusoidal waveforms," *IEEE Transactions on Power Electronics*, vol. 22, no. 1, pp. 30–40, 2007.

[12] H. Schierling, "Self-commissioning-a novel feature of modern inverter-fed induction motor drives," in *Third International Conference on Power Electronics and Variable-Speed Drives*. IET, 1988, pp. 287–290.

[13] L. Peretti and M. Zigliotto, "Automatic procedure for induction motor parameter estimation at standstill," *IET Electric Power Applications*, vol. 6, no. 4, pp. 214–224, 2012.

[14] E. Monmasson, *Power electronic converters: PWM strategies and current control techniques*. John Wiley & Sons, 2013.

[15] H. S. Patel and R. G. Hoft, "Generalized techniques of harmonic elimination and voltage control in thyristor inverters: Part i–harmonic elimination," *IEEE Transactions on Industry Applications*, no. 3, pp. 310–317, 1973.

[16] R. McElveen, M. Melfi, and J. McFarland, "Improved characterization of polyphase induction motor losses: Test standards must be modified to improve efficiency optimization," *IEEE Industry Applications Magazine*, vol. 25, no. 6, pp. 61–68, Nov 2019.

[17] P. Alger, *Induction Machines: Their Behavior and Uses*. Gordon and Breach, 1970. [Online]. Available: https://books.google.es/books?id=IO4eAQAAIAAJ

[18] W. Lo, C. C. Chan, Z.-Q. Zhu, L. Xu, D. Howe, and K. Chau, "Acoustic noise radiated by pwm-controllel induction machine drives," *IEEE Transactions on Industrial Electronics*, vol. 47, no. 4, pp. 880–889, 2000.

[19] M. Carbonieri, N. Bianchi, and L. Alberti, "Induction motor analysis using magnetostatic finite element simulations considering skewing," in *2019 IEEE International Electric Machines Drives Conference (IEMDC)*, May 2019, pp. 147–153.

[20] J. S. Hsu, "Monitoring of defects in induction motors through air-gap torque observation," *IEEE Transactions on Industry Applications*, vol. 31, no. 5, pp. 1016–1021, 1995.

[21] T. Jian, N. Schmitz, and D. Novotny, "Characteristic induction motor slip values for variable voltage part load performances optimization," *IEEE Transactions on Power Apparatus and Systems*, no. 1, pp. 38–46, 1983.

[22] H. Nejjari and M. E. H. Benbouzid, "Monitoring and diagnosis of induction motors electrical faults using a current park's vector pattern learning approach," *IEEE Transactions on industry applications*, vol. 36, no. 3, pp. 730–735, 2000.

[23] G. Joksimović, J. Riger, T. Wolbank, N. Perić, and M. Vašak, "Stator line current spectrum content of a healthy cage rotor induction machine," in *8th IEEE Symposium on Diagnostics for Electrical Machines, Power Electronics & Drives*. IEEE, 2011, pp. 113–118.

[24] J. Cameron, W. Thomson, and A. Dow, "Vibration and current monitoring for detecting airgap eccentricity in large induction motors," in *IEE Proceedings B (Electric Power Applications)*, vol. 133, no. 3. IET, 1986, pp. 155–163.

[25] S. J. Plathottam and H. Salehfar, "Induction machine transient energy loss minimization using neural networks," in *2016 North American Power Symposium (NAPS)*. IEEE, 2016, pp. 1–5.

Acknowledgments

Ringrazio la mia famiglia grazie al cui supporto é stato possibile realizzare tutto questo.
Il professor Nicola Bianchi per i preziosi consigli.
Quiero agradecer también al profesor Fernando Briz por su ayuda en el desarollo de esta tesis y a los colegas del grupo de investigación de accionamientos eléctricos y convertidores de potencia de la Universidad de Oviedo.